Earth and Planetary Science Letters 296 (2010) 165–180

Contents lists available at ScienceDirect

Earth and Planetary Science Letters

journal homepage: www.elsevier.com/locate/epsl

Testing models for post-glacial 'cap dolostone' deposition: Nuccaleena Formation, South Australia

Catherine V. Rose *, Adam C. Maloof

Department of Geosciences, Princeton University, Guyot Hall, Washington Road, Princeton, NJ 08544, USA

ARTICLE INFO

Article history:
Received 15 October 2009
Received in revised form 15 March 2010
Accepted 17 March 2010
Available online 16 June 2010

Editor: M.L. Delaney

Keywords:
cap dolostone
carbon isotopes
Ediacaran
Neoproterozoic
Nuccaleena Formation
snowball Earth

ABSTRACT

Sedimentologically and geochemically distinctive carbonate sequences consistently drape the glacial deposits associated with the younger Cryogenian ice age. The presence of ice-rafted debris in the basal dolostone implies that at least the lower portion of the cap sequence records deglaciation. An isochronous model proposes that cap dolostones were deposited synchronously around the world regardless of water depth, whilst a diachronous model proposes that deposition tracked glacioeustatic flooding during deglaciation. The Nuccaleena Formation of the Adelaide Rift Complex (ARC), South Australia, exhibits many of the unique sedimentary features observed in other younger Cryogenian cap dolostones around the world. Some bedforms are the product of wind-driven oscillatory flow, thus constraining post-glacial dolostone deposition to <400 m. These sedimentary features are absent in the deepest basinal facies in the northern ARC, suggesting that this region was below storm wave base even at the glacial sea level lowstand. In the north Flinders Ranges, there is a distinct relationship between lateral facies variability in the pre-, syn- and post-glacial sediments and the axes of 50 km scale structural folds. The northern fold limbs are characterised by basinal facies, whilst the southern limbs are associated with upper-slope facies. We interpret the abrupt facies transitions to reflect lower slope to upper slope/shelf breaks across a series of linked, south-facing half-grabens. The majority of cap dolostone carbon isotope records show monotonic declines in $\delta^{13}C$ of <2‰, with starting points between −0.5 and −3.5‰. An isochronous model implies a ~3.0‰ lateral gradient from platform to lower slope that varies dramatically on a short spatial scale and non-systematically with palaeobathymetry. If pre- and syn-glacial facies are used to infer palaeobathymetry, and cap dolostones are deposited diachronously as sea level rises during deglaciation, then $\delta^{13}C$ values becomes progressively lighter with time, implying that cap dolostone deposition tracked the glacioeustatic sea-level rise over a series of half-grabens that deepened to the north. The carbon isotope dataset cannot rule out uniquely isochronous or diachronous models. Given the high frequency spatial variability of $\delta^{13}C$ values, temperature cannot be the dominant control on the isotopic variability of the cap dolostone.

1. Introduction

Two Neoproterozoic (1000–542 Ma) glacigenic poorly-sorted conglomeratic units are present on all continents, often interrupting carbonate platform sequences, and sometimes found at the palaeomagnetic equator. Therefore, at least twice during this era, continental glaciers reached sea level in the low-latitudes (Embleton and Williams, 1986; Schmidt and Williams, 1995; Sohl et al., 1999; Evans, 2000; Macdonald et al., 2010). These two Cryogenian glaciations are generally referred to as the older 'Sturtian' and younger 'Marinoan' glaciations. Sedimentologically and geochemically distinctive carbonate sequences consistently drape both glacial deposits (Williams, 1979; Kennedy, 1996; Kennedy et al., 1998). These 'cap dolostones' are genetically linked with the glacigenic sediments based on their ubiquitous juxtaposition and the presence of ice-rafted debris within the basal dolostone (Hoffman et al., 1998). The younger Cryogenian cap dolostone (~635 Ma; Hoffmann et al., 2004; Condon et al., 2005) is laterally persistent in shelfal settings, blanketing the underlying syn-glacial sediments (Hoffman, 2005), and has been used as a lithological means to correlate the glacial units (Kennedy, 1996; Prave, 1999; Halverson et al., 2005). This cap dolostone is a laterally continuous buff to pink-coloured grainstone with a global average thickness of 18.5 m and is characterised by a unique set of sedimentary features, including isopachous sheet-crack cements, low-angle cross-stratified peloidal grainstones, pseudotepees, and vertical tube-like structures within 'plumb' stromatolites (Hoffman et al., 2007). In addition, the younger Cryogenian cap dolostone records a declining $\delta^{13}C$ isotopic trend, typically ranging between −1 and −3‰. This result implies that cap dolostones worldwide are the physical and chemical recorders of the greenhouse-driven disintegration of a snowball Earth (Hoffman et al., 1998, 2002, 2007; Higgins and Schrag, 2003).

* Corresponding author.
E-mail address: cvrose@princeton.edu (C.V. Rose).

0012-821X/$ – see front matter © 2010 Elsevier B.V. All rights reserved.
doi:10.1016/j.epsl.2010.03.031

1.1. Models for the carbon isotopic evolution of cap dolostones

Three models propose to explain the chemical evolution of cap dolostones: gas-hydrate destabilisation and methane oxidation (Kennedy et al., 2001; Jiang et al., 2003; Font et al., 2006), plumeworld (Shields, 2005), and the snowball Earth models (Hoffman et al., 1998, 2002; Higgins and Schrag, 2003). The origin of isotope variability within the cap dolostone has critical implications for the temporal constraints on its deposition. For each model, the temporal evolution of cap dolostone deposition has been variably interpreted as isochronous (Kennedy et al., 2001; Jiang et al., 2003, 2006; Font et al., 2006), semi-diachronous (Shields, 2005), and diachronous (Hoffman et al., 2007), respectively.

1.1.1. Isochronous

The gas-hydrate destabilisation and methane oxidation model proposes that organic-rich marine sediments were subaerially exposed by sea-level fall during the glaciation, and methane produced within the sediments was sequestered as clathrate in the resulting permafrost (Kennedy et al., 2001). The sea-level rise accompanying deglaciation warmed and destabilised the clathrates, causing cold methane seeps on the sea-floor to fuel microbial sulphate reduction that created alkalinity and stimulated the precipitation of carbonate (Kennedy et al., 2001; Jiang et al., 2003). This depositional mechanism is isochronous, meaning that the base and top of the carbonate sequence are the same age everywhere. Therefore, basin-wide dolostone records environmental changes synchronously during deglaciation, but after the post-glacial sea level rise, and would have been deposited at different water depths as a blanket on existing bathymetry. The $\delta^{13}C$ variability would reflect lateral and vertical gradients in ocean chemistry (Fig. 1A).

1.1.2. Semi-diachronous

The plumeworld model proposes that low latitude deglaciation was so extensive and abrupt that the resultant low density meltwater plume extended worldwide, physically separating the surface and deep ocean reservoirs for $>10^3$ years (Shields, 2005).In this hypothesis, cap dolostones are formed primarily by microbially mediated precipitation of carbonate whitings within a low salinity ocean rather than by abiotic precipitation from normal salinity seawater. For both the isochronous and semi-diachronous models, the deposition of the cap dolostone is not restricted to the time taken for deglaciation. Therefore, the semi-diachronous model requires that the base of the carbonate is diachronous and tracked the glacioeustatic transgression whilst the top of the sequence remains isochronous (Shields, 2005) (Fig. 1B).

1.1.3. Diachronous

The snowball Earth model proposes that a global glaciation caused extremely high levels of CO_2 to build up in the atmosphere (Hoffman et al., 1998, 2002). A super-greenhouse climate developed during deglaciation that resulted in acidic meteoric waters, combined with an intensified hydrological cycle, leading to rapid carbonate and silicate weathering. This weathering delivered vast quantities of alkalinity to the oceans, resulting in the rapid precipitation of carbonate (Hoffman et al., 1998, 2002). Higgins and Schrag (2003) suggested that the observed >2‰ drop in $\delta^{13}C$ of the younger Cryogenian cap dolostone can be explained by an increase in sea surface temperature that reduces the isotopic fractionation between CO_2 and carbonate.

This model proposes diachronous cap dolostone deposition where the base and top of the carbonate sequence varies in age depending on the palaeoelevation when it was deposited. Cap dolostone deposition would track rising sea-level and onlap on to the underlying sediments (Fig. 1C). As a result, the cap dolostone would be deposited within the same range of water depths everywhere, and $\delta^{13}C$ variability at different locations would reflect time evolution of post-glacial oceans. The timescale of deposition would be restricted to the time taken to melt continental ice sheets.

The depositional models make specific predictions about how the cap dolostones record the evolution of sea water temperature and chemistry during the deglaciation. Whichever model is more accurate, the rare but compelling presence of ice-rafted debris in the basal part of the cap dolostone implies that the cap records conditions during deglaciation. There have been two independent

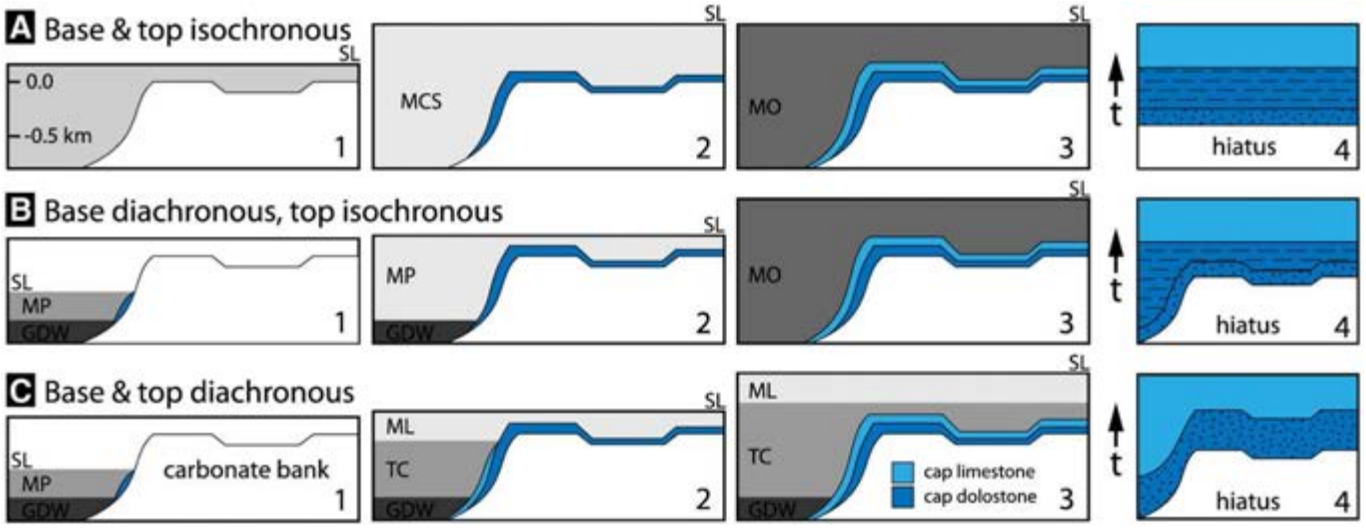

Fig. 1. Time-dependent models for post-glacial cap dolostone and limestone deposition (Hoffman et al., 2007). (A) Isochronous model: 1, depth–distance section during glacioeustatic rise, no carbonate deposited; 2, cap dolostone deposited in response to methane cold seepage (MCS) (Kennedy et al., 2001; Jiang et al., 2003, 2006); 3, cap limestone deposited in response to change in ocean chemistry (MO, mixed ocean; SL, sea level); 4, time–distance section of cap dolostone (dotted dark blue indicates shallow water, dashed dark blue indicates deeper water) and cap limestone (light blue). (B) Semi-diachronous model; 1, cap dolostone deposited from incipient meltwater plume (MP) above glacial deep water (GDW); 2, meltwater plume grows and floods the bank, cap dolostone deposited diachronously; 3, limestone deposited in response to mixing of MP and GDW (Shields, 2005); 4, time–distance section. (C) Diachronous model; 1, same as b1; 2, meltwater plume differentiates a mixed layer (ML), which deposits cap dolostone, and a thermocline (TC), which simultaneously deposits limestone; 3, TC floods the bank, causing diachronous change from dolostone to limestone at the ML–TC interface, an oxic–anoxic boundary in the meltwater column (Hurtgen et al., 2006); 4, time–distance section.

attempts to constrain timescale for deglaciation. Climate models predict rapid deglaciation within 2–10 kyr driven by ice albedo feedback, implying very rapid sedimentation rates of >2.0 cm yr^{-1} (Hyde et al., 2000; Peltier et al., 2004). In contrast, palaeomagnetic data show three polarity chrons in the South Australian and Brazilian cap dolostones, which predict a timescale for deglaciation of $>10^5$ yr (Trindade et al., 2003; Kilner et al., 2005; Raub and Evans, 2006; Schmidt et al., 2009).

Field mapping, sedimentology and $\delta^{13}C$ chemostratigraphy of the post-glacial 635 Ma Keilberg Formation (Fm) cap dolostone in northern Namibia has been used to differentiate between diachronous and isochronous models, and to propose a time-evolution story for the post-glacial ocean (Hoffman et al., 2007). This work concluded that the sedimentological and geochemical observations support the diachronous model for cap dolostone deposition. However, the diachronous and isochronous models are yet to be tested on other palaeocontinents.

The ~635-Ma Nuccaleena Fm cap dolostone in South Australia has the most robust younger Cryogenian glacial constraints on palaeolatitude of any Neoproterozoic glacial deposit (Sohl et al., 1999; Raub and Evans, 2006; Schmidt et al., 2009) and is spectacularly exposed across the Adelaide Rift Complex (ARC; Preiss, 1987; Fig. 2A). Although we cannot use a simple palaeobathymetric model of an isolated carbonate platform to quantify palaeo-water depths across the ARC due to complicated palaeogeography and active salt diapirism, this palaeomargin is still an ideal location to test cap dolostone diachroneity across a range of water depths and sedimentary environments at 7–14° latitude (Sohl et al., 1999; Raub and Evans, 2008; Schmidt et al., 2009). In this paper, we present detailed sedimentological observations and $\delta^{13}C$ data of the Nuccaleena Fm cap dolostone from 41 sections across the ARC. We aim to test the concept that the Nuccaleena Fm was deposited during deglaciation, and differentiate between diachronous and isochronous models for its deposition in order to constrain the evolution of carbon isotopes in post-glacial oceans.

2. Geological background

The ARC is thought to be part of an extensive continental margin formed to the present-day east of the Stuart Shelf (Preiss, 2000; Fig. 2A). Palaeoproterozoic to Mesoproterozoic cratonic basement is overlain by a 7–12 km thick Neoproterozoic to Cambrian sedimentary package that is subdivided into four units: the Callanna, Burra, Umberatana and Wilpena Groups (Preiss, 1987, 2000). The ARC was a zone of deep subsidence, punctuated by episodes of syn-sedimentary faulting and diapiric mobilisation of Callanna Group evaporites (Preiss, 1987; Fig. 2B). Neoproterozoic sediment accumulation is attributed to a succession of rift and thermal subsidence phases, with the main rifting commencing at ~827–802 Ma (Fanning et al., 1986; Jenkins, 1990; Wingate et al., 1998).

The fold belt is subdivided into four main structural domains; the southern Adelaide Fold-Thrust Belt, the Nackara Arc, the central Flinders Ranges, and northern Flinders Ranges. In this paper, the Nackara Arc and southern Adelaide Fold-Thrust Belt will be referred to collectively as the south Flinders Ranges. The south and central Flinders Ranges represent the least-deformed part of the ARC. In contrast, the northern Flinders Ranges are dominated by broad, south-verging open folds (McLaren et al., 2002).

2.1. Stratigraphy of the Adelaide Rift Complex

The Burra Group consists of basal carbonates with evaporites and clastics, whilst glacimarine deposits and post-glacial sequences characterise the younger Umberatana and Wilpena Groups, respectively. This succession is followed by transgressive Early Cambrian shallow-marine sandstones and deeper water carbonates and shales (Preiss, 1987). Deposition terminated and the sedimentary rocks were folded during the Cambro-Ordivician Delamerian orogeny to create a region of elevated topography forming the Flinders and Gammon Ranges (Thomson et al., 1964).

The Nuccaleena Fm is the dolostone unit that caps the youngest Cryogenian glacial unit in the ARC. This cap dolostone is tentatively dated by correlation of its distinct lithofacies to the uppermost younger Cryogenian glacial deposits and the similar sedimentary structures in associated cap dolostones in Oman (Bowring et al., 2007; Rieu et al., 2007), Namibia (Hoffmann et al., 2004) and South China (Condon et al., 2005), which contain U–Pb zircons dated at ~635 Ma. The Nuccaleena Fm is stratigraphically bound by the Etina, Enorama, Trezona/Yaltipena and Elatina Fms below and the Brachina Fm above. The Etina Fm consists of shallow marine sandstone, oolites and microbial reefs. The base of the Enorama Fm shale marks a major flooding surface, followed by a coarsening and shallowing upward sequence, culminating in intraclastic limestone breccias, stromatolite bioherms, oolitic grainstones and siltstones of the Trezona Fm. The Yaltipena Fm overlies and may be partly contemporaneous with the Trezona Fm and contains fine terrigenous sandstones and siltstones with mudcracks and rain imprints, indicating intermittent subaerial exposure. The overlying syn-glacial Elatina Fm exhibits impressive facies variability, from debris flows and turbidites to ice-contact tillites and laminated siltstones (Coats, 1981; Preiss, 1987; Eyles et al., 2007). The Elatina–Nuccaleena Fm contact marks the onset of the post-glacial transgression, the base of the Wilpena Group (Williams, 1977; Plummer, 1979; Dyson, 1992; Kennedy, 1996) and the beginning of the Ediacaran Period (Knoll et al., 2006) (Fig. 2B).

3. Methods

Carbonates were sampled at ~0.2 m resolution while measuring 41 individual stratigraphic sections. Clean dolostones and limestones without siliciclastic components, secondary veining or cleavage were targeted. A total of 1280 samples were slabbed and polished perpendicular to bedding and 5 mg of powder were micro-drilled from individual laminations for isotopic analysis. $\delta^{13}C$ and $\delta^{18}O$ data were acquired simultaneously on a VG Optima dual inlet mass spectrometer attached to a VG Isocarb preparation device in the Stable Isotope Laboratory at the University of Michigan. Approximately 1 mg aliquots of powder were reacted in a common, purified H_3PO_4 bath at 90 °C for 8–10 min. Evolved CO_2 was purified and collected cryogenically, and then analysed against an in-house reference gas. The analytical uncertainty (1σ) of this measurement was less than 0.05‰ for ^{13}C. Samples were calibrated to VPDB (Vienna Pee Dee Belemnite) using six measurements of the Cararra Marble standard for each run of 54 samples. Memory effect associated with the common acid bath system was minimised by increasing the reaction time for dolomite samples and monitoring the measured values of standards. Examination of the variation in standards after each run showed that the error due to memory effect was always <0.2‰.

4. Sedimentology

Throughout the ARC, the Nuccaleena cap dolostone is a laterally continuous layer of buff, pale tan or pinkish dolomite. It ranges in thickness from <1 m to 33 m and preferentially thickens towards the north. The lower contact of the cap dolostone can be gradational with red siltstone (Raub et al., 2007) or display a sharp contact, and may include clasts typically derived from winnowed lags of the underlying Elatina diamictite. The upper contact of the Nuccaleena Fm is conformable and lithologically gradational into predominantly red siltstone, or limestone in the far north (Fig. 2A; sections 38 and 39). Occasionally, the dolostone becomes progressively interbedded with siltstone and nodular dolostone in red siltstone across 1–13 m. The

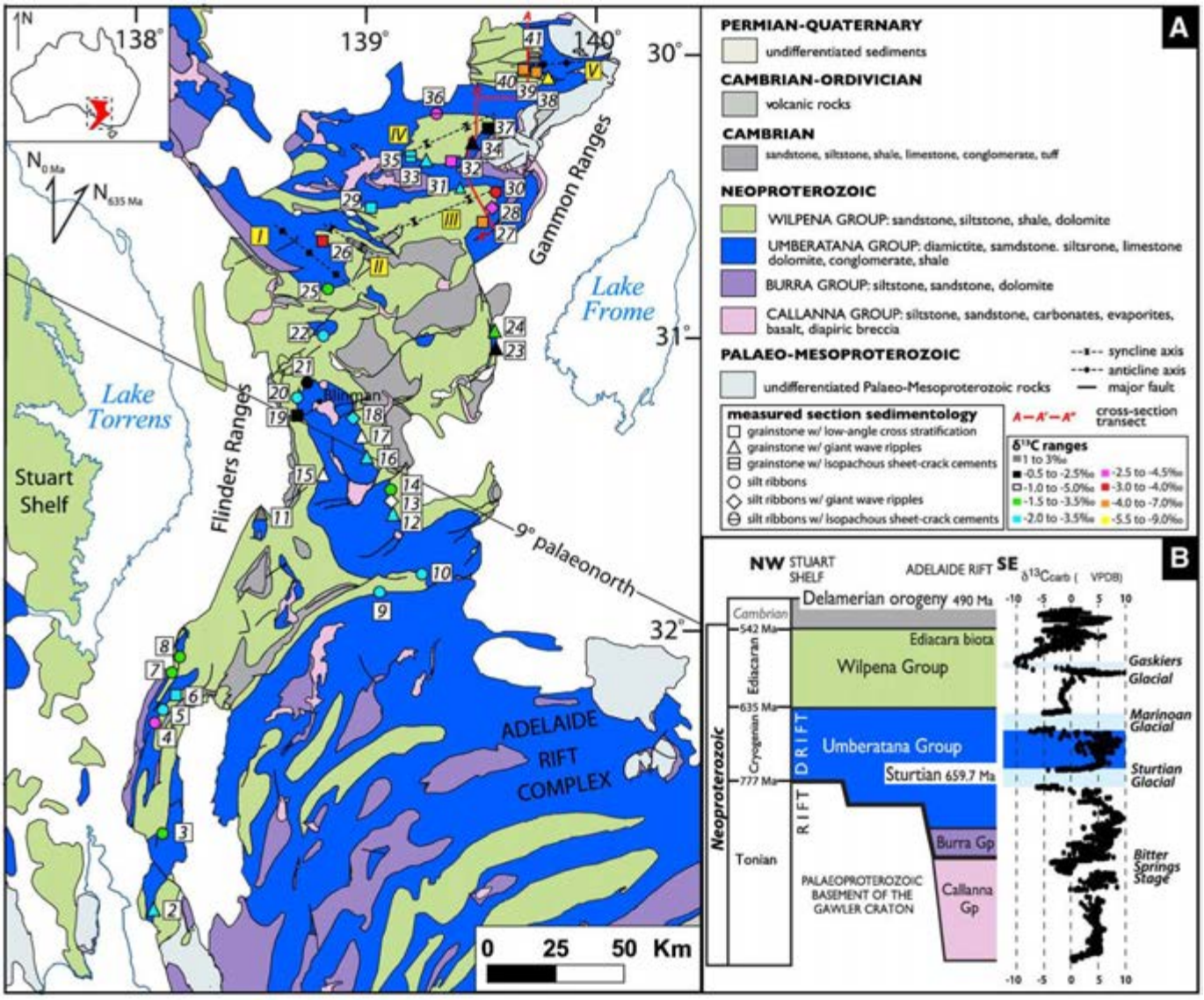

Fig. 2. (A) Simplified geological map of the study area within the Adelaide Rift Complex (ARC) (adapted from Preiss and Robertson, 2002). Locations of measured stratigraphic sections are denoted by red circles and labeled with numbered squares. Fold axes within the Adelaide Rift Complex are denoted by dashed lines and labeled with Roman numerals: (I) Mount Morris anticline; (II) Mount Jeffery syncline; (III) Arkaroola syncline; (IV) Umberatana syncline; and (V) Mount Fitton anticline. The line of the cross-section A–A′–A″ in Fig. 5 is denoted by a solid red line. (B) Schematic NW–SE stratigraphic cross-section of the Adelaide Rift Complex, highlighting the rift-to-drift transition and major sequence boundaries (adapted from Lemon and Gostin, 1990). $\delta^{13}C$ profile adapted from Halverson et al. (2005) time-aligned with the right-hand edge of the stratigraphic cross-section. A SHRIMP U–Pb zircon age of 659.7 ± 5.3 Ma from a tuffaceous horizon in the Wilyerpa Fm, just above the Appila (Sturtian) diamictite, may provide a maximum age for the base of the interglacial sediments (Fanning, 2006). The Nuccaleena Fm is dated by correlation to the uppermost Marinoan glacial deposits and the associated cap dolostone in Oman (Bowring et al., 2007; Rieu et al., 2007), Namibia (Hoffmann et al., 2004) and South China (Condon et al., 2005), which contain ID TIMS U–Pb zircon ages of ~635 Ma.

last appearance of dolostone defines the top of the Nuccaleena Fm (Lemon and Gostin, 1990).

4.1. Facies stratigraphic distribution

The Nuccaleena Fm consists of four lithofacies: low-angle cross-stratified dolomite grainstones, grainstones with pseudo-tepees, red silty dolomite ribbons, and dolomite ribbons with isopachous sheet-crack cements (Fig. 3A–E). 'Ribbon' facies consists of low-angle cross-stratified, swaley dolosiltite.

4.1.1. Cross-stratified grainstones and large bedforms

The most widespread facies is buff or pale tan dolomite grainstone which is characterised by fine to medium grains, mm-scale laminae, often with small-scale swaley, low-angle cross-stratification (Fig. 3A). This facies is similar to that documented in correlative cap dolostones on other palaeocontinents, where it often contains normally and reverse graded peloids (Kennedy, 1996; James et al., 2001; Halverson et al., 2004; Xiao et al., 2004; Font et al., 2006; Jiang et al., 2006).

The cross-bedded grainstones generally are associated with distinctive metre-scale sedimentary structures documented previously in the Nuccaleena Fm and other correlative cap dolostones (Allen and Hoffman, 2005; Hoffman et al., 2007; Hoffman and Li, 2009) (Fig. 3B). These bedforms typically are referred to as 'pseudo-tepees' and display trochoidal profiles with curved troughs and sharp near-symmetrical crests with bidirectional cross-stratification in their crestal regions (Allen and Hoffman, 2005). Their synoptic relief from crest to trough is ~50 cm and individual ripple trains aggrade to create distinctive sigmoidal climbing crests in cross-section. The sigmoidal climbing crests occur when sediment is deposited on both sides of the ripple during rapid aggradation under the influence of wave action.

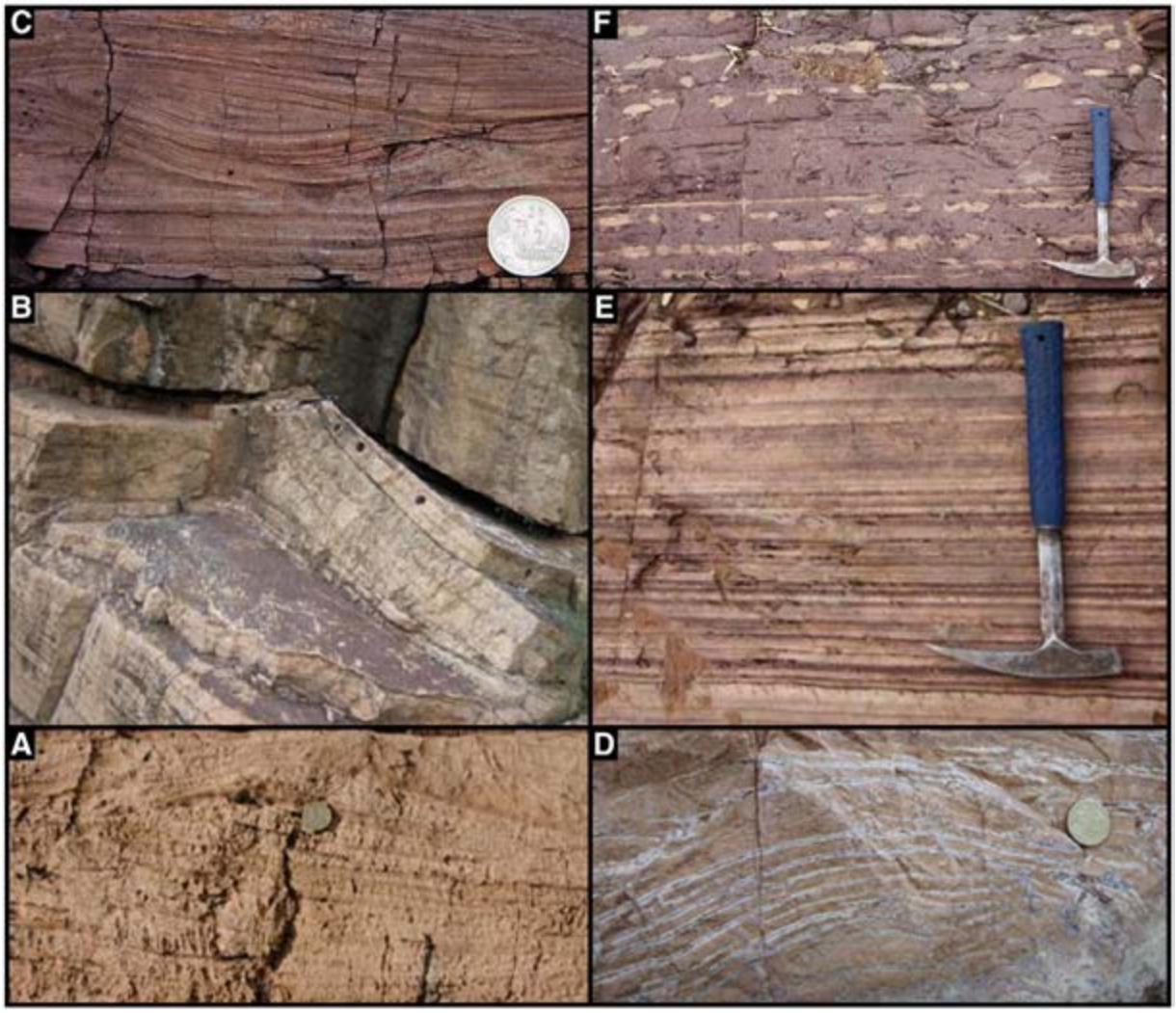

Fig. 3. The Nuccaleena Fm consists of several distinct lithofacies that can be divided into two groups based on their common field associations. In stratigraphic order, the first group consists of (A) low-angle cross-stratified dolomite grainstone, Emu Gap, (B) grainstone with a cross-section of a pseudo-tepee, Elatina Creek, and (C) red silt to fine sand with swaley cross-stratification of the Brachina Fm, Partacoona. These facies are found throughout the Central and South Flinders Ranges, and on the southern limb of folds in the North Flinders Ranges. The second laterally equivalent lithofacies group consists of (D) dolomite ribbons with isopachous sheet-crack cements, Lame Horse Gully, (E) red silty dolomite ribbons, South Pinnacle Bore, and (F) nodular dolostone in red silt, Pettana Creek. The sheet-crack cements are only found on the northern limbs of folds in the North Flinders Ranges.

In plan view, the linear crestlines are parallel to one another, with a mean crestal azimuth 002° ($n = 50$), and are uniformly spaced 1.0–3.6 m apart within a given bed (Aitken, 1991; James et al., 2001) (Fig. 4A). The pseudo-tepees occur preferentially in the upper part of the cap dolostone sequence within the grainstone facies. The host grainstones are overlain by dark red-brown siltstone-fine sandstone of the Brachina Fm (Fig. 3C). On rare occasions, the bedforms may exhibit brecciation at their apex and bedform steepness that exceeds the angle of repose.

4.1.2. Silty ribbons and sheet-crack cements

Red silty dolomite ribbons are also common facies that are characterised by mm-scale parallel and low-angle laminae (Fig. 3E). This facies typically occurs in the upper part of the Nuccaleena Fm, but in places may constitute entire stratigraphic sections of the cap dolostone. The silty ribbons grade into flaggy lenticular and nodular dolostone in red silts (Fig. 3F). Associated with siltstone ribbons that occur at the base of the Nuccaleena Fm are isopachous sheet-crack cements (Fig. 3D). The sheet-cracks are typically parallel to bedding and filled by fibrous, isopachous quartz or dolomite cement. The basal zone of sheet-cracks is sometimes folded and may vary in crack density, but remains laterally continuous at outcrop and even map scales.

4.1.3. Comparison with other cap dolostones

The Nuccaleena Fm hosts three unique features that have not been reported in other younger Cryogenian cap dolostones. Small, asymmetric bedforms with amplitudes between 3 and 10 cm are often present in the upper metres of both the cross-bedded grainstones and red silty dolomite ribbons (Fig. 4E,F). These bedforms are typically individual structures but may also be present in groups of 2–4 with a wavelength ~0.1–0.5 m. The bedform steepness varies between 5 and 15° and the crests are linear for at least 1 m and trend 350–010°. These structures do not contain void filling cements but may exhibit brecciated crestlines (Fig. 4E,F). In addition, the individual laminae can vary in thickness over the crestlines (Fig. 4B). All crests are onlapped by very fine grainstone (Fig. 4B). Within the cross-bedded grainstone facies, these bedforms typically culminate in pseudo-tepees.

Load structures and tabular clast breccias have not been documented previously in other cap dolostones around the world, but are present in the silty dolostone ribbon facies in the south and central regions of the ARC. Syn-sedimentary faults, ball and pillow loading structures and water-escape features record significant soft-sediment deformation in the silty ribbon facies in the South Flinders Ranges (Fig. 4I,J). These features are typically restricted to an ~80 cm layer

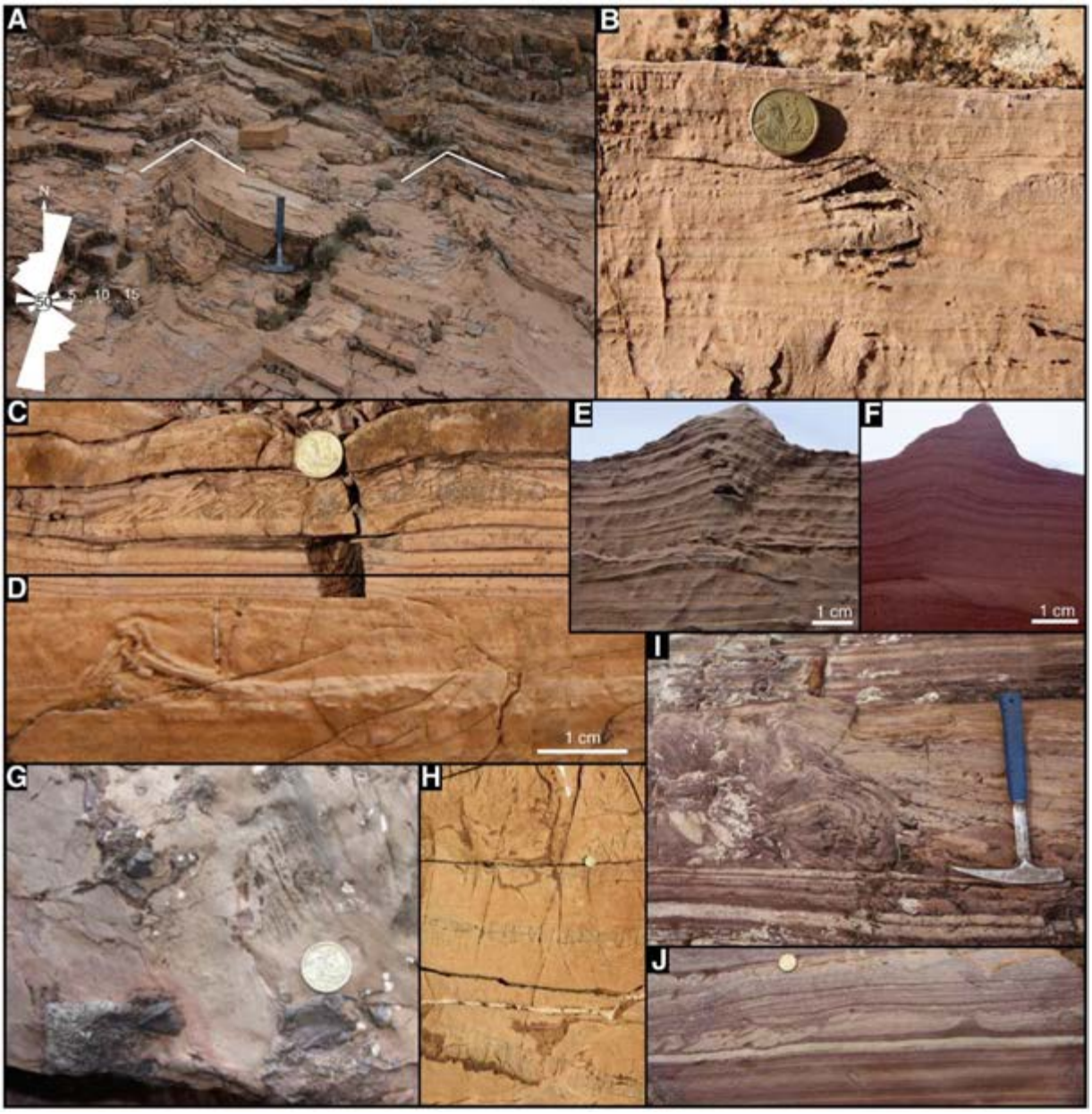

Fig. 4. Sedimentary features within the Nuccaleena Fm cap dolostone. (A) The crestlines of pseudo-tepees in plan view are consistently linear and parallel to one another with a mean crestal azimuth 002° ($n = 50$), Mt. Curtis. (B) Small, asymmetric bedforms in cross-bedded grainstone, Emu Gap. (C) Lens of tabular grainstone clast breccia within silt dolomite ribbons, South Pinnacle Bore. (D) Asymmetric bedform with brecciated crest and rucked-up folded tabular clasts at the centre, Wearing Gorge. (E) Cross-section of small, asymmetric bedform in cross-bedded grainstone. (F) Same bedform as (E) showing lack of cements. (G) Ice-rafted debris within the basal Nuccaleena Fm, Trezona Bore. (H) Small 10 cm fining upwards parasequences that begin with sharp contacts with cm-scale scours and load structures, East Mundawertina. (I) Soft-sediment deformation within the silt ribbon facies, Pettana Creek. (J) Tabular clast breccia and water escape structure within silty dolostone ribbons, Pettana Creek.

in the upper part of the cap dolostone and are bound by parallel laminated to low-angle cross-stratified silty dolostone ribbons. The breccias occur as isolated lenses of vertically imbricated, flat ~2 cm dolostone clasts that are oriented at sub-vertical angles (Fig. 4C,J). The lenses pinch out on a 10 cm scale and are often laterally associated with soft-sediment deformation (Fig. 4I,J). These soft-sediment deformation features occupy the usual stratigraphic level of pseudo-tepees in the grainstone facies.

4.2. Geographic distribution of facies

There is a broad lateral facies change in the Nuccaleena Fm and underlying stratigraphy from the south to the north. The pre-glacial Trezona Fm and equivalents show a northward transition from thick mud-cracked sandstone and siltstone deposits in the south (Yaltipena Fm), to stromatolites and limestone breccias in the central region, and grey-green calcareous shales in the north. The overlying glacigenic Elatina Fm transitions from marine sands in the south, to ice-contact tillites in the central region, and debris flows and turbidites in the north. The isopachous sheet-crack cements within the Nuccaleena Fm are restricted to the northern Flinders (Fig. 2A).

Within the central and southern Flinders Ranges, abrupt lateral facies changes occur on <1 km scales that are not linked to similar transitions in the underlying stratigraphy. For example, on the east limb of the central fold around Blinman (Fig. 2), the Nuccaleena Fm transitions from ~5 m of buff grainstone to ~17 m of red silty dolomite ribbons over a distance of ~500 m (Emu Gap—South Pinnacle Bore; Fig. 10B). To the north in the Gammon Ranges, there

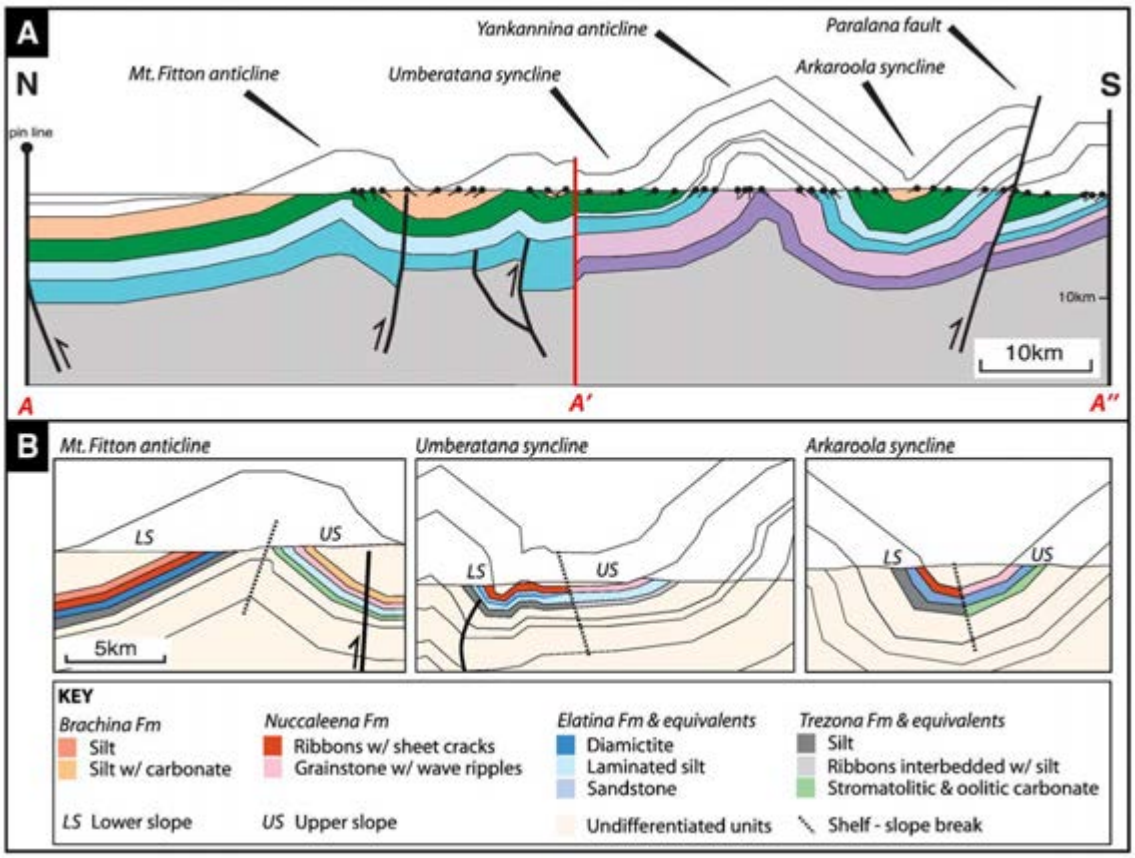

Fig. 5. (A) Balanced composite cross-section through the northern Flinders Ranges (adapted from Paul et al. (1999)). The red line labelled A′ represents a break in the section line (A–A′–A″ in Fig. 2). Refer to Fig. 2 for the legend of the geological units. (B) Schematic cross-sections of the three folds illustrating the repeated lithology transitions across the fold axes, which are interpreted to represent the shelf-slope break.

is a distinct and predictable relationship between lateral facies variability in the pre-, syn- and post-glacial sediments and the axes of three 50-km scale structural folds (Fig. 5). The Nuccaleena Fm consists of winnowed dolomite grainstones with pseudo-tepees to the south of the fold axes, while dolomite grainstones or ribbons with isopachous sheet-crack cements are found to the north (Fig. 5). These facies variations are consistently linked to similarly abrupt changes in the lithology of the underlying pre- and syn-glacial stratigraphic units. The pre-glacial Etina Fm records grainstones and stromatolite facies south of the fold axis and siltstone, shale and olistostromes to the north (Coats et al., 1973; Giddings and Wallace, 2009). Similarly, the younger Trezona Fm and equivalent facies transition from siltstone and limestone ribbons on the southern fold limb to turbidites on the northern limb (Coats et al., 1973). The syn-glacial facies change from laminated siltstones and rarer boulder tillites on the southern fold limbs to conglomeratic debris flows, diamictites, and massive gritty siltstones on the northern limbs.

The northern Mt. Fitton anticline shows the same abrupt facies changes across the fold axis in the pre-, syn- and post-glacial formations. However, the Nuccaleena Fm displays some notable differences. South of the fold axis, the Nuccaleena Fm consists of 10 cm beds that begin with sharp contacts, cm-scale scours and load structures (Fig. 4H). The beds consist of brown dolomite cross-bedded grainstone that fines upward into grey dolomite micrite. The upper contact of the Nuccaleena Fm remains conformable and grades, not into red siltstone, but into ~19 m of grey limestone ribbons that outcrop along the entirety of the southern panel of the fold. The Nuccaleena Fm on the northern limb also is a ~30 m thick package of dolomite with pervasive isopachous sheet-crack cements throughout the lower 20 m. Above 20 m, there is a notable change to less silicified carbonate with a mottled texture reminiscent of late-dolomitisation of limestone. We suggest that this transition is the contact between primary (or very early diagenetic) dolostone and primary limestone that has subsequently been dolomitised.

5. Carbon isotopes

5.1. South and central Flinders Ranges

The $\delta^{13}C$ trends for individual sections in the south Flinders Ranges start between −1 and −2.5‰ and each record a monotonic decline of ~2‰ (Fig. 6). The carbon isotope records within the central region are similar to those in the south but have a wider range of starting values between −1 and −3.5‰ and have less steep trajectories (Fig. 7).

5.2. North Flinders Ranges

The north Flinders Ranges $\delta^{13}C$ isotope records show a declining trend, with starting values between −0.5‰ and −5‰ (Fig. 8). The $\delta^{13}C$ values become progressively lighter towards the north from Walter's Well (Fig. 2A). Superimposed on this general trend, the isotope values across each individual fold in the northern ARC are lightest on the southern limb and become progressively heavier towards the north (Figs. 8 and 9).

The Arkaroola syncline $\delta^{13}C$ isotope trends begin between −2‰ and −3.5‰, with the starting value becoming progressively heavier across the fold towards the north (Figs. 8C and 9). The Umberatana syncline $\delta^{13}C$ values have similar isotope ranges, and become progressively higher towards the north. The Mt. Saturday isotope

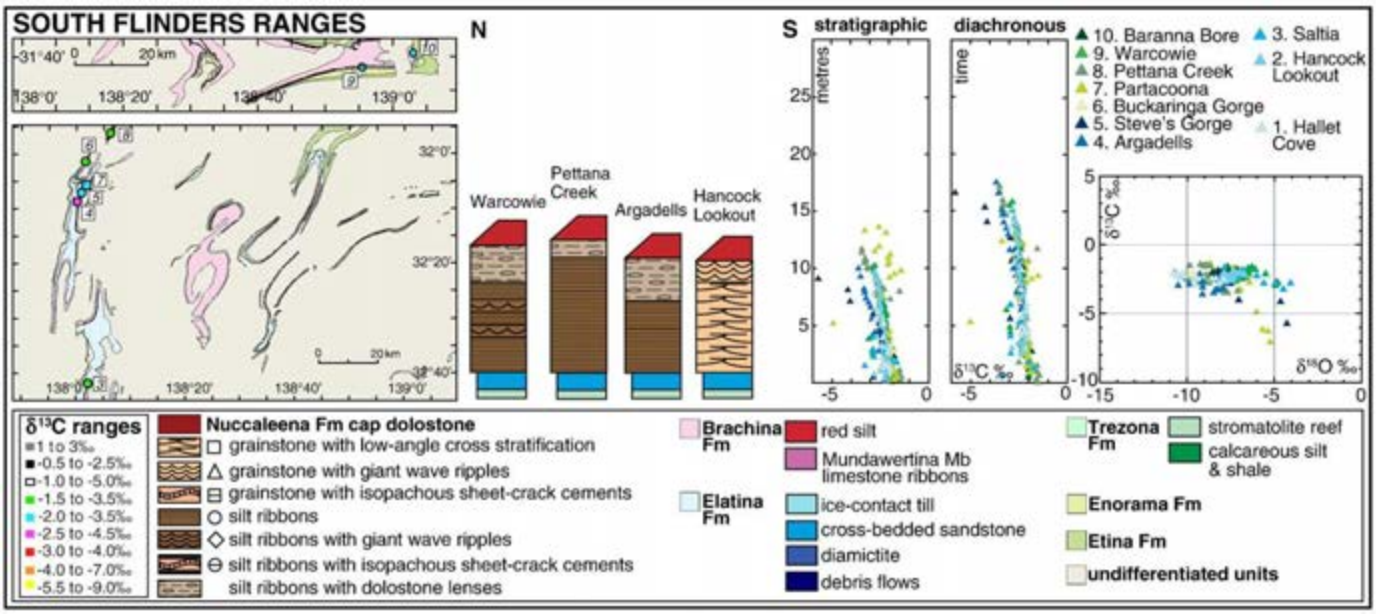

Fig. 6. Representative stratigraphic sections and carbon isotope profiles for the Nuccaleena cap dolostone within the south Flinders Ranges. The symbols on the map mark the locations of the sections: shape represents the lithology of the cap dolostone, whilst the colour refers to the $\delta^{13}C$ value of the basal carbonate sample in the section. The raw carbon isotope data are plotted against stratigraphy and $\delta^{18}O$ values in the cross-plot. In addition, assuming a diachronous model, the stretched carbon isotope data are plotted where the decreasing trend represents the *relative* timing of deposition. Note that the *y*-axis for the data plotted using the diachronous model represents the *relative* timing of cap dolostone deposition based on isotope values.

record begins at −0.5‰ and is on average 1‰ heavier than any of the other records (Figs. 8C and 9).

The Mt. Fitton anticline records distinctly different $\delta^{13}C$ isotope trends when compared to other cap dolostone sections within the ARC and around the world. The three sections on the southern fold limb record depleted isotope values from −5 to −8.5‰ (Figs. 8A and 9). West Mundawertina has a notably large range of $\delta^{13}C$ values and a gentle negative slope. The other sections record scattered $\delta^{13}C$ values near the dolostone–limestone transition, but average around ≃ 7.5 above ~15 m.

6. Discussion

6.1. Sedimentology

Three observations of the Elatina–Nuccaleena contact suggest that there is not a low-angle unconformity on outcrop scale (Forbes and Preiss, 1987; Preiss, 2000; Williams et al., 2008). Firstly, the basal Nuccaleena Fm contact does not display an angular cross-cutting relationship in any of the 41 measured sections. Secondly, the Elatina Fm remains a remarkably constant thickness ranging

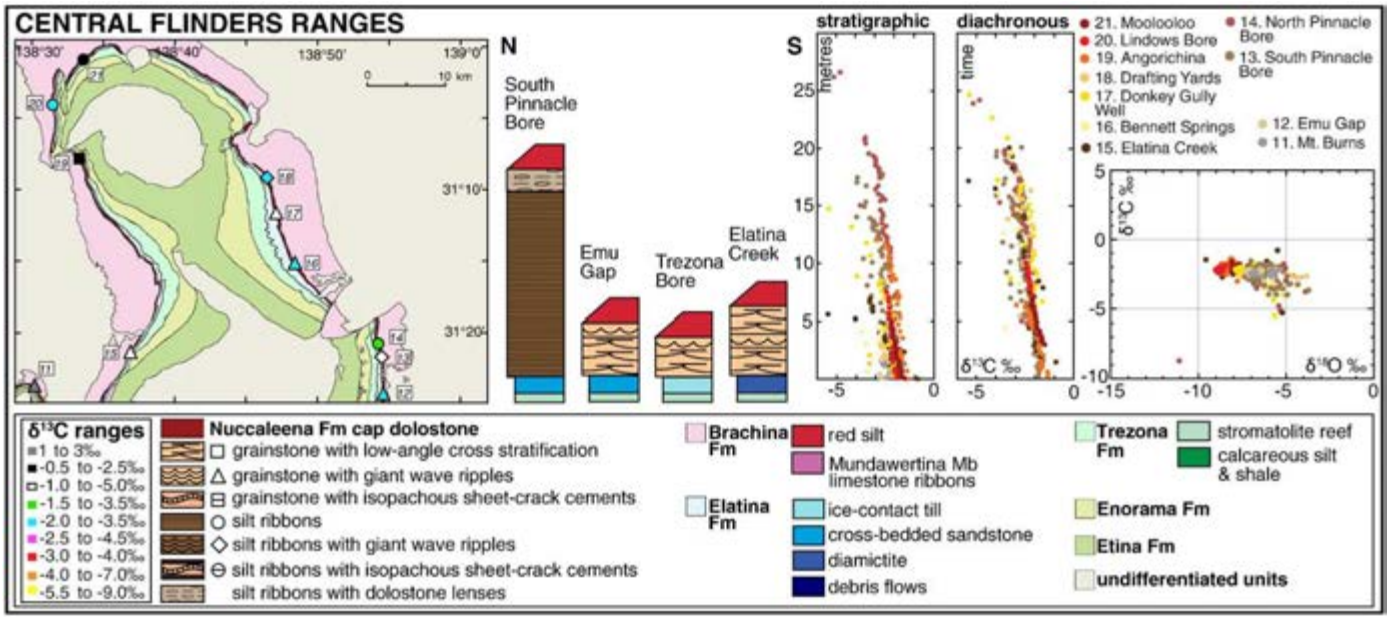

Fig. 7. Representative stratigraphic sections and carbon isotope profiles for the Nuccaleena cap dolostone within the central Flinders Ranges. The symbols on the map mark the locations of the sections: shape represents the lithology of the cap dolostone, whilst the colour refers to the $\delta^{13}C$ value of the basal carbonate sample of the section. The raw carbon isotope data are plotted against stratigraphy and $\delta^{18}O$ values in the cross-plot. In addition, assuming a diachronous model, the stretched carbon isotope data are plotted where the decreasing trend represents the *relative* timing of deposition. Note that the *y*-axis for the data plotted using the diachronous model represents the *relative* timing of cap dolostone deposition based on isotope values.

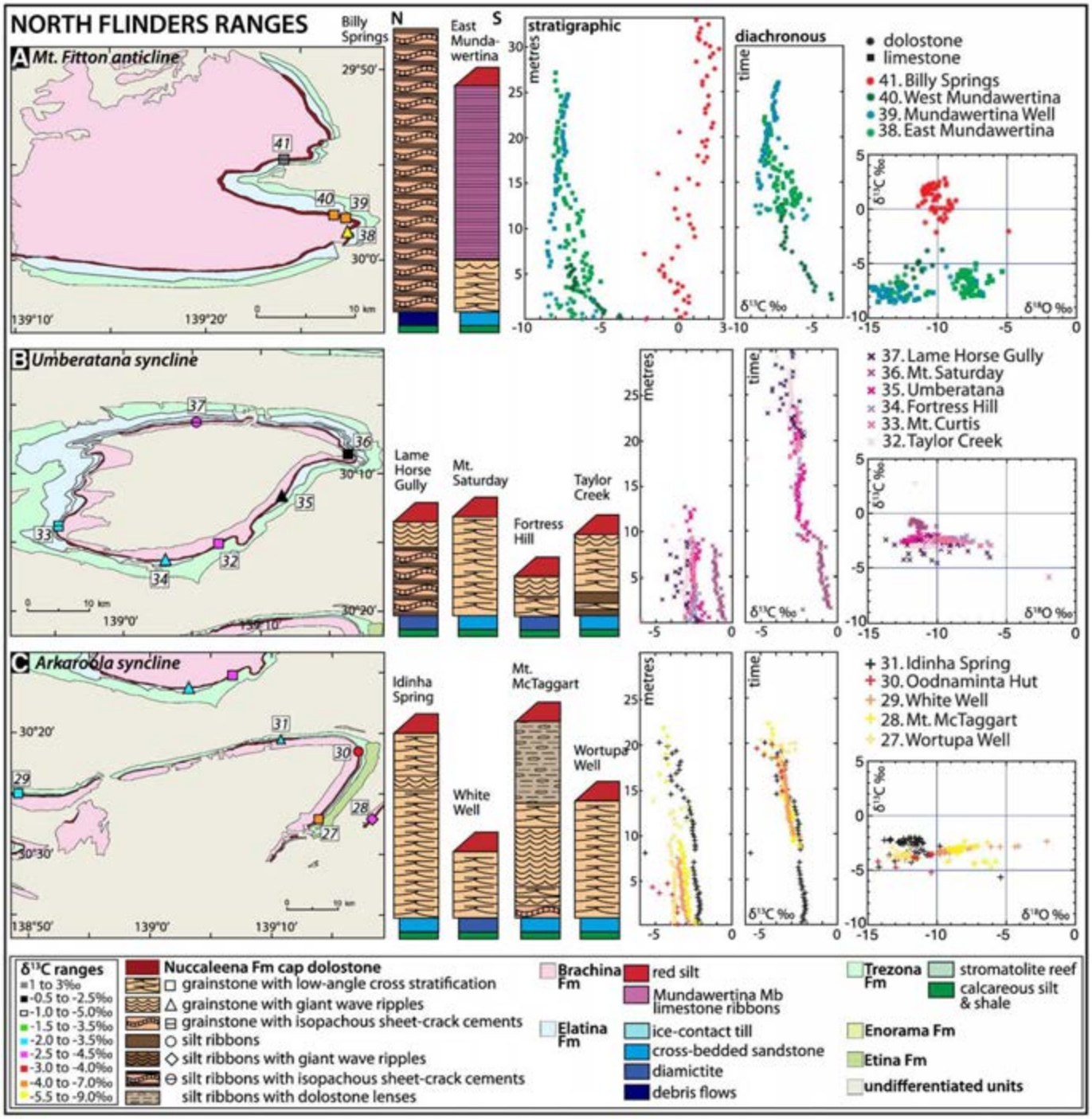

Fig. 8. Representative stratigraphic sections and carbon isotope profiles for the Nuccaleena cap dolostone within the north Flinders Ranges. The symbols on the map mark the locations of the sections: shape represents the lithology of the cap dolostone, whilst the colour refers to the $\delta^{13}C$ value of the basal carbonate sample of the section. The raw carbon isotope data are plotted against stratigraphy and $\delta^{18}O$ values in the cross-plot. In addition, assuming a diachronous model, the stretched carbon isotope data are plotted where the decreasing trend represents the *relative* timing of deposition. Note that the *y*-axis for the data plotted using the diachronous model represents the *relative* timing of cap dolostone deposition based on isotope values. N.B. The Billy Springs data were not plotted using the diachronous model because the positive $\delta^{13}C$ values make it hard to stretch the record against the reference section and its placement would be highly subjective.

between ~70 and 100 m. Thirdly, the contact may be winnowed, knife sharp, or transitional with silt and ice-rafted debris (Fig. 4G). This variably sharp contact may suggest the presence of a local disconformity between the two formations. However, although it is uncertain as to how much time is missing in each section, it is known that the basal cap carbonate was deposited when glaciers were present. Therefore, there is no unconformity with respect to the ice age.

In addition, previous work describes laminated, pale buff dolostone characteristic of the Nuccaleena Fm being intertongued with the Seacliff Sandstone (Forbes and Preiss, 1987; Dyson, 1992; Preiss, 2000). However, this relationship was not observed in the South, Central or North Flinders. The Trezona, Yaltipena, Brachina, and even Elatina Fms have rare buff dolostone and limestone beds that superficially resemble the Nuccaleena Fm, but when examined more closely, have unique sedimentology and $\delta^{13}C$ profiles (Calver, 2000).

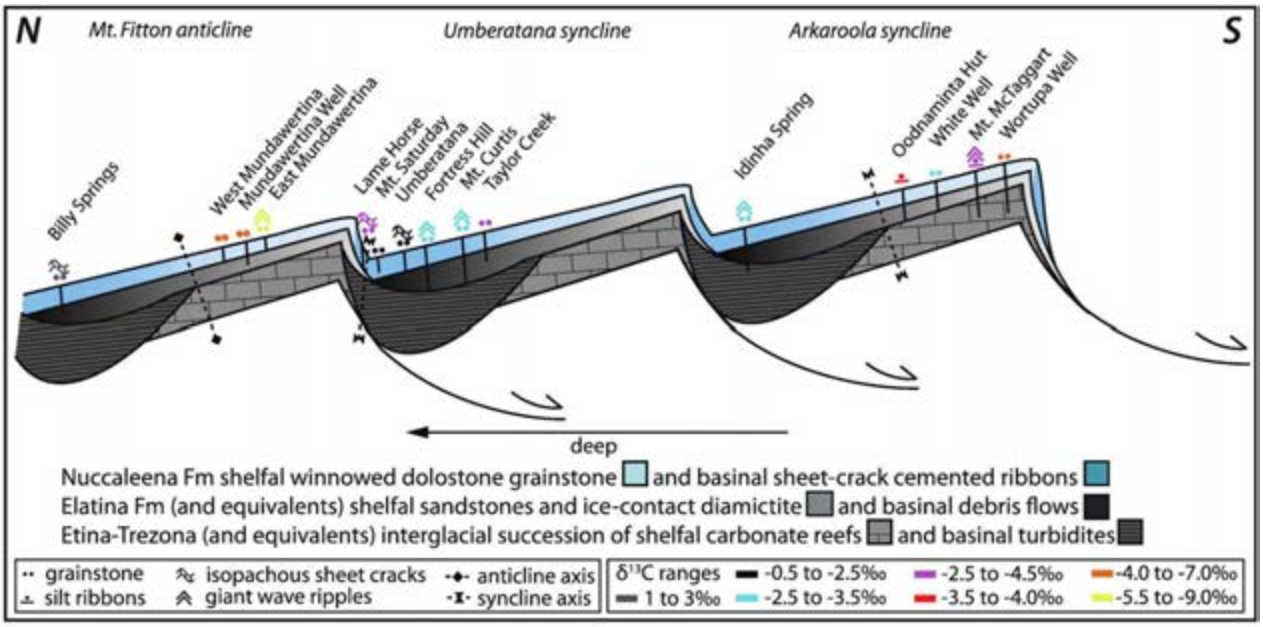

Fig. 9. Schematic cross-section illustrating the relationship between abrupt lateral facies variability in Etina/Trezona-, Elatina- and Nuccaleena-equivalent formations and the axes of 50 km scale structural folds (figure is not to scale). These abrupt lateral changes are interpreted as reflecting the lower-upper slope break across a series of linked, south-facing half grabens. Measured stratigraphic sections are denoted by lithofacies symbols used in Fig. 10 that are colour-coded by their $\delta^{13}C$ isotopic ranges. The length of the vertical line below represents the formations that were measured. The axes of the structural folds are denoted by black dashed lines.

These nondescript dolostone beds lack the distinct lateral continuity, unique set of facies and bedforms, and declining carbon isotopic trend that have been observed worldwide in the younger Cryogenian cap dolostone.

6.1.1. Grainstone and 'giant wave ripple' facies

The presence of low-angle cross-stratified grainstones and normal- and reverse-graded laminae in the Nuccaleena Fm are similar to those described in correlative cap dolostones on other palaeocontinents (James et al., 2001; Hoffman et al., 2002, 2007; Halverson et al., 2004; Xiao et al., 2004; Fig. 3A), and are indicative of symmetric wave ripples, bidirectional flow and deposition above normal wave-base in a dynamic wave-dominated regime (Hoffman et al., 2007).

Three hypotheses have been put forward to explain the origin of pseudo-tepees. Numerous workers propose that these bedforms have an external morphology and internal structure identical to that of intertidal tepee structures formed through expansive crystallisation during early diagenesis (Plummer, 1979; Aitken, 1991; Kaufman et al., 1997; Gammon et al., 2005). Gammon et al. (2005) argue that paired tepee and growth fault structures demonstrate that the pseudo-tepees grew 3.5–7.1 m below the sediment–water interface. Alternatively, Kennedy (1996) suggests that these features share morphological and petrographic attributes with modern and ancient methane seeps, in which methane gas and fluids provide both a force for physical disruption from buoyancy and a source of alkalinity for significant carbonate cementation from sulphate reduction (Jiang et al., 2003, 2006).

Allen and Hoffman (2005) propose that the common symmetrical trochoidal form and bidirectional cross-lamina near the pseudo-tepee crests are consistent with 'giant wave ripples' (Fig. 3B). Individual bedforms have been documented to aggrade continuously for <1.5 m of stratigraphy, which implies high sedimentation rates of accumulation under steady wave conditions (Allen and Hoffman, 2005). Allen and Hoffman (2005) relate the large ripples to surface gravity waves and attribute their distinct characteristics to oscillatory flow with flow separation over the bedform crest and asymmetric aggradation with each half-cycle of the wave motion. Their hydrodynamic analysis suggests that the bedforms formed in 200–400 m water under the influence of long period waves generated by sustained wind with unlimited fetch (Allen and Hoffman, 2005). The occurrence of ripples in the upper part of the cap dolostone is attributed to their formation near storm wave-base, where only the longest-period waves agitate the bottom. In shallower water, the interference from shorter period waves is too great to allow bedforms associated with long-period waves to develop in the lower part of the cap sequence in a diachronous model. Hoffman et al. (2007) suggest that the presence of giant wave ripples constrains the range of water depths for cap dolostone deposition, regardless of where they are found on the slope or platform. Jerolmack and Mohrig (2005) support this ripple interpretation, but attribute the bedform amplitude to be indicative of deposition by hurricane winds generating a wave base <40 m, which require only hours to aggrade. However, Allen and Hoffman (2005) noted that the crestal azimuths of successive ripple trains do not vary more that 15° possibly supporting an origin by sustained zonal winds with consistent orientation (Hoffman and Li, 2009).

Throughout the ARC, the pseudo-tepees are not associated with void filling cements like true tepees and do not create polygonal networks in plan view (Kendall and Warren, 1987) (Fig. 4A). In fact, azimuth data from the linear crests of pseudo-tepees within the Nuccaleena Fm indicate a dominant north–south trend (mean direction 002°, $n=50$) across the ARC. This preferred orientation is very hard to explain if the bedforms are tepees. The undisturbed internal lamination is unambiguously sedimentary in origin and the bedforms are consistent with giant wave ripples that record oscillatory flow during rapid aggradation (Allen and Hoffman, 2005; Hoffman et al., 2007; Hoffman and Li, 2009). The variably positive, negative, or inconclusive palaeomagnetic fold tests throughout the Nuccaleena Fm suggest that the ripples began as primary structures that were subsequently deformed (Schmidt et al., 2009). We suggest that the rare faults, core brecciation (Gammon et al., 2005) and bedform steepness that exceeds the angle of repose represent secondary deformation. The wave ripple interpretation constrains the water depth for cap dolostone deposition across the ARC. We propose that the giant wave ripples are generally absent in the north

because palaeowater depths were >400 m, and to the south because water depth was <200 m throughout the interval of glacioeustatic rise. The ripple interpretation does not definitively constrain the timescale for deposition. Multiple magnetic reversals recorded in the cap dolostone indicate a much longer time for cap dolostone deposition than it would take to deposit a 1.5 m ripple with extremely fast aggradation (Raub and Evans, 2008). In Elatina Creek, red <1 mm thick shaley laminae representing stylolites (insoluble residues from pressure dissolution) or clay drapes do not correlate with the magnetic reversals or jumps in $\delta^{13}C$ values, suggesting that hiatuses do not reconcile the timescale disparity. Thus, the duration of cap dolostone deposition remains an unresolved problem.

The dominant north–south trend of the crestlines across a variety of palaeo-bathymetric locations corroborates the zonal wind hypothesis proposed by Hoffman and Li (2009). Assuming wind directions were perpendicular to the ripple crestlines, palaeomagnetic latitude and orientation of the Australian continent are consistent with easterly trade winds (Schmidt et al., 1991, 2009; Sohl et al., 1999; Raub and Evans, 2008). When the crest azimuth data are grouped by region, the data from the northern Flinders Ranges accounts for most of the variability in the crestline orientations. A stronger dispersion in the data may reflect a combination of wave refraction, Eckman forcing in subsurface waters, or palaeotopographic effects on surface winds (Hoffman et al., 2007). Although the data are consistent with the zonal wind interpretation, the northern region faced an open ocean and the variable wind directions might be more consistent with hurricanes, while the central region may have been within an embayment that refracted and guided incoming waves. This hypothesis is corroborated by the current understanding of local palaeogeography with land to the west and the Gawler and Curnamona Cratons creating a large embayment that deepened to the north (Preiss, 1987, 2000).

6.1.2. Silt ribbons and sheet-crack cement facies

The very low angle cross-lamination within the thin-bedded silty dolostone ribbons is consistent with a setting above the storm wave base that lacked coarse sediment. In the northern Flinders Ranges on the northern fold limbs, this facies is intimately associated with isopachous sheet-crack cements (Fig. 3D). Kennedy et al. propose that the sheet-crack cements originate from methane produced in sediments being sequestered as hydrate in permafrost. In this model, post-glacial transgression destabilises these methane clathrates and leads to gas escape causing brecciation and bedding expansion (Kennedy, 1996; Kennedy et al., 2001; Jiang et al., 2003). In addition, these workers identify cements with evidence of subaerial exposure in the glacial diamictite below. The strongest field evidence for such gas-escape structures is found at Hallet Cove in the southern ARC, where distinctive vertical cemented 'chimneys' and sparry calcite cements are present in the syn-glacial Elatina Fm coarse sandstone (Kennedy et al., 2008).

Hoffman (2010) poses an alternative explanation for the sheet-crack cements based on the observation that the cements filled voids that opened vertically, normal to sedimentary layering, implying that pore-fluid over-pressure overcame the hydrostatic load. One way to reduce the hydrostatic pressure more rapidly than the pore-fluid pressure can adjust is a rapid fall in sea level (Hoffman, 2010). The Keilberg Fm, Namibia, consistently begins with cm-scale dololutite turbidites which are overlain by peloidal dolostone with low-angle cross-stratification (Hoffman, 2010). This fall in base-level has been attributed to the loss of gravitational-pull on the adjacent ocean accompanying the collapse of an ice-sheet, and provides an explanation for the opening of the associated sheet-cracks (Hoffman, 2010). The void-filling cements must then be precipitated fast enough to prevent the collapse of the cracks due to the imminent glacioeustatic rise following the local ice-sheet's disappearance.

Our work corroborates the observation that isopachous sheet-crack cements are typically associated with deep water foreslope facies, but their origin remains ambiguous. Unlike permafrost methane cold seeps, the sheet-cracks in the Nuccaleena cap dolostone are laterally persistent on outcrop and map scales and do not form centred complexes. We never observed disruption of the underlying strata expected with methane originating from below the cap dolostone, except perhaps at Hallet Cove. Evidence for ice-contact glacial deformation within the Elatina Fm diamictite is never associated with sheet-crack cements in the Nuccaleena Fm above. Furthermore, the sheet-cracks were not observed to be associated with the vertical tube structures that Kennedy et al. have attributed to methane release. Overall, all the identified bedforms lack the size, chaotic internal bedding, carbonate crust and concretionary morphologies of cold seep structures (Gammon et al., 2005). However, neither does the Nuccaleena cap dolostone contain basal turbidites below the sheet-crack cements, which typically directly overlie the glacial diamictite. Therefore, despite there being neither clear evidence to support subaerial exposure and permafrost nor a fall in base level during deglaciation, methane is common in present day deep sea and slope settings and may be related to the origin of sheet-crack cements.

6.1.3. Other sedimentary features

The previously undocumented small asymmetrical bedforms lack void filling cements that are indicative of true tepees (Fig. 4E,F). Although the linear crestlines are not exposed for more than ~1 m, they are all orientated between 350 and 010°, which is not only uncharacteristic for a random polygonal network of tepees, but is also the same preferred orientation as the giant wave ripples. Furthermore, true tepees are associated with exposure surfaces, yet these features are always bound by uninterrupted swaley, low-angle cross-stratified grainstone, often with normal- and reverse-graded laminae. These facies are consistent with storm wave-dominated deposition and complement the strong evidence that cap dolostones record a continual post-glacial transgression. The often solitary bedforms may be incipient ripples which, if not destroyed by shorter period waves, eventually culminate into giant wave ripples. These ripples would form at the ripple-to-dune transition where there are anomalies on the bed that trigger changes in the response of the sediment bed to turbulence, which often further amplifies the resulting dune. Their solitary presence could be a result of patchy early cementation that prevented their destruction.

The silty dolomite ribbon facies often includes soft-sediment deformation and tabular clast breccias (Fig. 4I,J). The presence of syn-sedimentary faults, ball and pillow loading structures and water-escape features attest to rapid sedimentation rates, loading, and fluid overpressure. The silt facies may help to reduce the permeability and increase pore fluid pressure, whilst at the same time preventing granular flow and ripple formation, and thus may explain why this facies hosts soft-sediment deformation and not ripples. Tabular clast breccias may represent regions that are being winnowed by alternating currents generated by waves that cause the dolomite to break up into lenticular clasts and tilt up against obstacles or within scoured depressions in the shore platform (Myrow et al., 2004). This tilting allows the clasts to lodge in the sediment beneath and initiate vertical packing. The tabular clast breccias and small, asymmetrical bedforms both occupy the upper half of the Nuccaleena cap dolostone stratigraphy and may be formed by the same processes. The presence of rucked-up folded clasts at the centre of some of the small, asymmetrical bedforms suggests that the breccias may represent an irregularity in the bed needed for the initiation of a ripple (Fig. 4D). The silt could have provided cohesiveness that prevented the sediments from forming incipient ripples within the silty dolomite ribbons.

6.1.4. Lateral facies variability

There is local and regional scale lateral facies variability within the ARC. Facies throughout the central Flinders Ranges vary over a short <1 km spatial scale. The entire North Pinnacle Bore section (Fig. 10B)

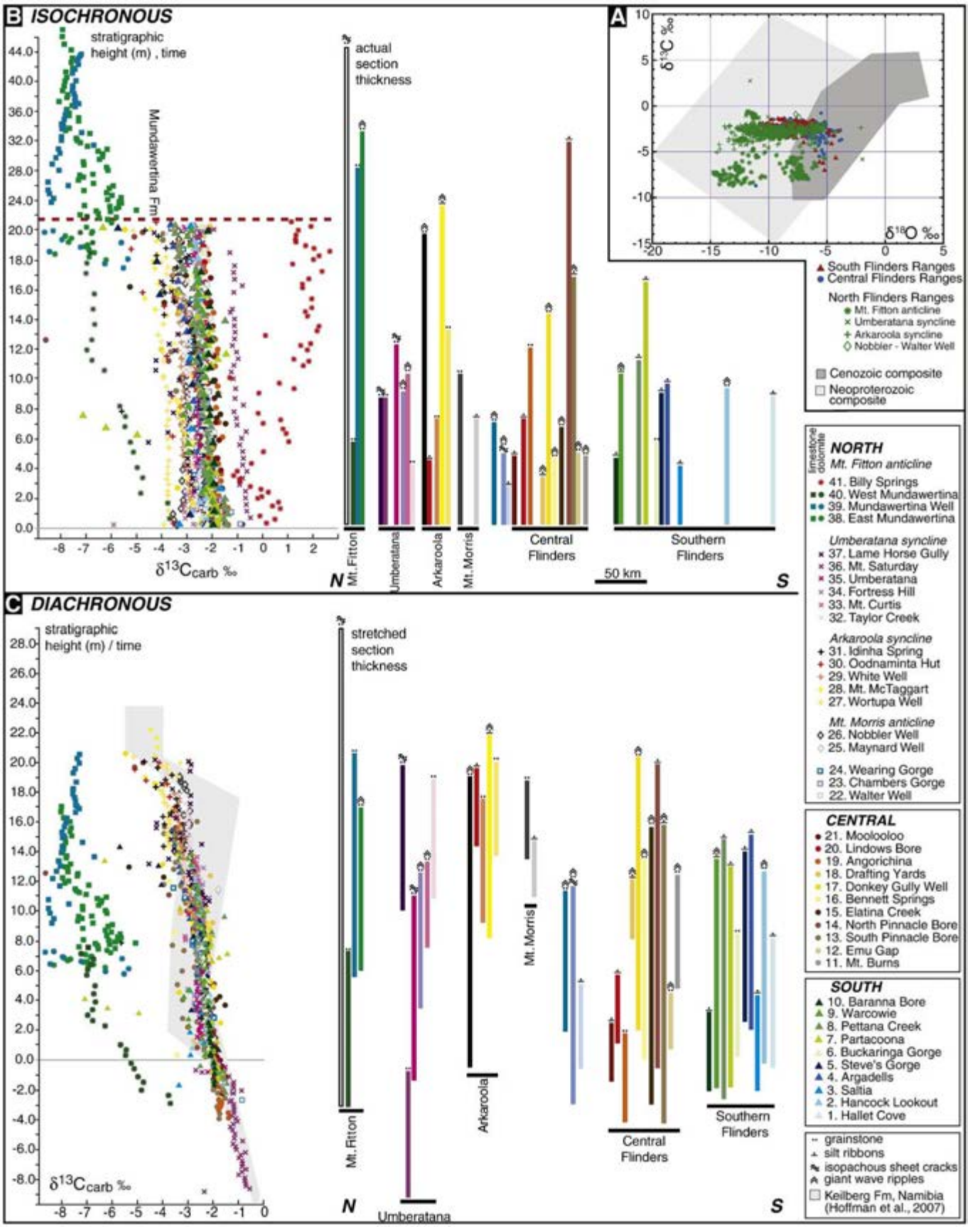
B ISOCHRONOUS
stratigraphic height (m) , time
Mundawertina Fm
actual section thickness
δ13Ccarb ‰
N
Mt.Fitton
Umberatana
Arkaroola
Mt.Morris
Central Flinders
Southern Flinders
50 km
S
A
δ13C ‰
δ18O ‰
South Flinders Ranges
Central Flinders Ranges
North Flinders Ranges
Mt. Fitton anticline
Umberatana syncline
Arkaroola syncline
Nobbler - Walter Well
Cenozoic composite
Neoproterozoic composite
limestone dolomite
NORTH
Mt. Fitton anticline
41. Billy Springs
40. West Mundawertina
39. Mundawertina Well
38. East Mundawertina
Umberatana syncline
37. Lame Horse Gully
36. Mt. Saturday
35. Umberatana
34. Fortress Hill
33. Mt. Curtis
32. Taylor Creek
Arkaroola syncline
31. Idinha Spring
30. Oodnaminta Hut
29. White Well
28. Mt. McTaggart
27. Wortupa Well
Mt. Morris anticline
26. Nobbler Well
25. Maynard Well
24. Wearing Gorge
23. Chambers Gorge
22. Walter Well
CENTRAL
21. Mooloolo
20. Lindows Bore
19. Angorichina
18. Drafting Yards
17. Donkey Gully Well
16. Bennett Springs
15. Elatina Creek
14. North Pinnacle Bore
13. South Pinnacle Bore
12. Emu Gap
11. Mt. Burns
SOUTH
10. Baranna Bore
9. Warcowie
8. Pettana Creek
7. Partacoona
6. Buckaringa Gorge
5. Steve's Gorge
4. Argadells
3. Saltia
2. Hancock Lookout
1. Hallet Cove
C DIACHRONOUS
stratigraphic height (m) / time
stretched section thickness
δ13Ccarb ‰
N
Mt.Fitton
Umberatana
Arkaroola
Mt.Morris
Central Flinders
Southern Flinders
S
grainstone
silt ribbons
isopachous sheet cracks
giant wave ripples
Keilberg Fm, Namibia (Hoffman et al., 2007)

consists of siltstone ribbon, yet less than 1 km to the north and south are giant wave ripples in grainstone. Moreover, the presence of siltstone ribbons is independent of the lateral variations in the underlying stratigraphy. Therefore, the dolomite ribbons were not deposited below or significantly above the storm wave base. One possible explanation for this rapid lateral and thickness variability is that the red silty dolostone ribbons record point sources of fluvial sediment influx. This hypothesis is consistent with the observation that most of the Nuccaleena silt content occurs in the south where water depths are shallow and there is the thickest underlying Yaltipena Fm sediments located nearest the glacial sediment source.

The northern Flinders Ranges is structurally different from the south, consisting of south verging-open folds that are intimately associated with regional facies changes. Paul et al. (1999) partly attribute this pattern to the thickness and rheology of the sedimentary package, which significantly thins to the north. We propose that the sedimentary facies and the presence of basin-bounding normal faults influenced the deformation to create the distinct relationship between lateral facies variability in the pre-, syn-, and post-glacial stratigraphy and the axes of the folds (Fig. 5). The transition from shallow platform to deep basinal facies across the Arkaroola syncline axis in the Etina sediments already has been documented (Coats et al., 1973; Preiss, 1987; Giddings and Wallace, 2009). Giddings and Wallace (2009) interpreted this pre-glacial facies variation to mark a reef margin to slope setting. We agree with this interpretation during deposition of the Etina Fm across the Arkaroola syncline, and further suggest that the abrupt lateral facies changes in subsequent formations and those across the folds to the north represent the transition from the outer ramp or upper slope to the lower slope (Fig. 9). During Cambro-Ordovician folding and thrusting, steep graben bounding normal faults likely were reactivated as reverse faults, generating structures above them whose axes reflect the ancient position of the lower slope–upper slope break.

6.2. Carbon isotopes

6.2.1. Diagenesis

Diagenetic overprinting of original seawater isotopic signatures is always a concern in ancient carbonates. In fact, some workers claim that all Neoproterozoic carbon isotope data are diagenetically altered (Knauth and Kennedy, 2009). However, it is unlikely that the isotopes across the ARC were considerably altered because: 1) mm-scale sedimentary textures are extremely well preserved, 2) the $\delta^{13}C$ values record reproducible coherent isotopic signals with minimal scatter over meters, kilometers and hundreds of kilometers, and 3) the $\delta^{13}C$ values of the underlying Trezona and Etina Fm carbonates are reproducible at both a 1 km and 100 km spatial scale. Kaufman et al. (1991) proposed covariation in $\delta^{13}C$ and $\delta^{18}O$ as an index for differentiating between pristine and adulterated $\delta^{13}C$ values in altered samples. However, the level of diagenetic alteration across the ARC would be porosity- and permeability-dependent, and given the variable sedimentological data, the $\delta^{13}C$ and $\delta^{18}O$ data would be scattered when plotted against stratigraphy. Furthermore, the majority of $\delta^{13}C$ and $\delta^{18}O$ cross-plots for ARC data show a lack of covariation and near invariance in $\delta^{13}C$ values with respect to large changes in $\delta^{18}O$ (Figs. 6–8).

Higher degrees of visible recrystallization and amphibolite grade metamorphism suggest that the northern outcrops might have been diagenetically altered. The Oodnaminta Hut section in the Arkaroola syncline does record higher than predicted $\delta^{13}C$ isotope values that show slight scatter and covary with $\delta^{18}O$ values. This locality is in close proximity to a fault zone that could have been associated with local fluid flow that altered the $\delta^{13}C$ and $\delta^{18}O$ records (Fig. 8C). However, this explanation is only valid when looking at the Oodnaminta section in isolation. It is not a satisfactory explanation for the isotope trend across the Arkaroola syncline, because all the other sections within the fold show tight and consistent $\delta^{13}C$ trajectories inconsistent with alteration being the cause of the anomalous $\delta^{13}C$ depletion. The high levels of reproducibility and tight stacking of $\delta^{13}C$ profiles within fold structures on 1–100 km spatial scales and complete lack of porosity- and permeability-controlled $\delta^{13}C$ scatter do not support the diagenesis model. Furthermore, the absolute values and range of $\delta^{13}C$ values of the Nuccaleena Fm are similar to other cap dolostones around the world, arguing against local diagenesis.

6.2.2. Isochronous model

The isochronous model proposes that cap dolostones were deposited like a blanket on the sea floor, such that all outcrops are laterally and temporally equivalent. Assuming such an isochronous model, Higgins and Schrag (2003) proposed that the ~2‰ monotonic decline in $\delta^{13}C$ values seen in other younger Cryogenian cap dolostones around the world is indicative of an increase in sea surface temperature. Today, the temperature-dependence of carbon isotope fractionation is insignificant because, at a pH of 8.2, the equilibrium fractionation between HCO_3 and CO_3^{2-} is small (−1.5‰ at 25 °C). However, at pH <7.3, CO_2 (gas) becomes the dominant aqueous carbon species and its equilibrium fractionation with CO_3^{2-} at 25 °C is +6.3‰. Therefore, with CO_2 being dominant over CO_3^{2-} in a post-glacial ocean, any change in fractionation due to temperature will be expressed as a change in the $\delta^{13}C$ of CO_3^{2-}. As temperature rises, the fractionation becomes smaller and the $\delta^{13}C$ of CO_3^{2-} will decline.

To test the isochronous model across the ARC, all isotope records are normalised to a common thickness (Fig. 10B). Idinha Spring was selected as the reference section because it was deposited low on the slope and records nearly the full range of the $\delta^{13}C$ record. Using experimentally derived values for temperature-dependent isotopic fractionation, a 12 °C change in temperature could explain the average 1.4‰ temporal gradient recorded in the Nuccaleena Fm. This change in sea surface temperature with time does not seem implausible in a high CO_2 world. However, the simultaneous precipitation of the Nuccaleena cap dolostone also would record lateral gradients in $\delta^{13}C$ values for the duration of deposition. The lateral gradient across the Arkaroola syncline is 1.6‰ per 20 km, whilst the gradient across the Umberatana syncline is 2.2‰ per ~30 km (Fig. 10B). A ~30 °C change in temperature would be required to account for the ~3.4‰ difference between the lightest and heaviest $\delta^{13}C$ starting values in the ARC. These isotopic gradients are unrealistically steep, whether representing temperature or not, and do not vary systematically with palaeobathymetry of the underlying facies. The presence of giant wave ripples implies rapid and deep mixing, making it improbable for lateral gradients in $\delta^{13}C$ values to exist, let alone be maintained for the duration of cap dolostone deposition.

Fig. 10. (A) Cross-plot of $\delta^{18}O$ vs. $\delta^{13}C$ for the North, Central and South Flinders Ranges, Adelaide Rift Complex. The dark and grey shaded boxes represent Cenozoic and Neoproterozoic data composites (Knauth and Kennedy, 2009). (B) Colour-coded composite $\delta^{13}C$ records for the Nuccaleena cap dolostone using the isochronous model. Sections are not stretched and the true thickness of the sections is shown by colour bars which are separated by a scaled north–south distance between sections. (C) Colour-coded composite $\delta^{13}C$ records for the Nuccaleena cap dolostone using the diachronous model. All sections are normalised to the thickness of the Idinha Spring section. These stretched thicknesses are shown by colour bars which are aligned to their stacked isotope records. The red line denotes the transition from dolostone to limestone which represents the boundary between the Nuccaleena Fm and Mundawertina Fm. Note that the *y*-axis for the data plotted using the diachronous model represents the *relative* timing of cap dolostone deposition based on isotope values. The sections with the lowest colour-coded bars represent those which would have flooded first. Hence, for each individual fold structure the *x*-axis represents time, but collectively, sections that occur at the same heights would be flooding simultaneously. N.B. The Billy Springs data were not plotted using the diachronous model because the positive $\delta^{13}C$ values make it hard to stretch the record against the reference section and its placement would be highly subjective.

The isotope values recorded across the Mt. Fitton anticline are anomalous. East Mundawertina records extremely negative $\delta^{13}C$ values suggesting diagenesis and possible complete filling of primary pore space of the turbiditic grainstone with ^{13}C-depleted marine cements that formed at great depth near the base of the slope. In contrast, the Billy Spring section records the most ^{13}C-enriched isotope trend for any cap dolostone in the world. It is possible that this anticline represents the rare preservation of dolostone in a very deep setting that records the onset of deglaciation before global sea level rose significantly. An all inclusive hypothesis to explain both the depleted and enriched isotopic values across the Mt. Fitton anticline would be that in the deepest setting, methanogenesis generated isotopically heavy bicarbonate where the cap was precipitating *in situ* (with sheet-cracks). However, migration and subsequent oxidation of the methane upslope would produce light dissolved carbon that could be incorporated into the pore filling cement, resulting in grainstone with a very light isotopic signature. However, new $\delta^{13}C$ data from the cements show the $\delta^{13}C$ values to be similar to, if not heavier than, those of the bulk carbonate, requiring that the cement and dolomite be homogenised or that the deep methanogenesis hypothesis is incorrect (see Supplementary online material). The Billy Springs results from Mt. Fitton are significant, but remain enigmatic.

6.2.3. Diachronous model

The diachronous model proposes that cap dolostone deposition tracked glacioeustatic flooding during deglaciation such that the $\delta^{13}C$ trends record the evolution of ocean chemistry over time (Fig. 10C). Based on the trajectory of each individual section and the patterns observed in the Namibian cap dolostone (Hoffman et al., 2007), $\delta^{13}C$ should decrease with time in this model, and each individual section should record some time slice of this isotopic decline. We can predict that the $\delta^{13}C$ starting points for each isotope record should show a similar, small-scale trend within each half-graben, where $\delta^{13}C$ start values become isotopically lighter in shallower water locations that were inundated later during glacioeustatic rise (Fig. 9). To test the diachronous model, all $\delta^{13}C$ isotope records are stretched and aligned to fit part of the Idinha Spring reference section (Fig. 10C). This correlation results in a series of 'stacked' isotope records that are interpreted to be deposited progressively with time.

The $\delta^{13}C$ values across the folds in the North Flinders Ranges document the most compelling evidence to support a purely diachronous model across a series of south-facing linked half-grabens (Fig. 10C). The sections on the southern limb of the Arkaroola syncline align with one another near the top of the Idinha Spring section on the northern limb (Fig. 10C). The Idinha Spring section flooded before all the sections on the southern limb, which were deposited broadly synchronously. An abrupt change in slope between the north and south fold limbs would explain this pattern, which supports previous interpretations that the facies transition represents the shelf to slope break on the southern limb (Coats et al., 1973; Giddings and Wallace, 2009).

The Umberatana syncline records the heaviest isotopes, as well as the largest isotope range in the ARC (Fig. 8B and 10C). The southern limb of the syncline records a systematic progression of $\delta^{13}C$ isotopes for each section that get lighter towards the south. The isotopes stack to create a steep temporal gradient that, assuming constant rates of sedimentation, may either be interpreted as a steep paleao-slope gradient and/or a relatively slower rate of sea level rise. Nearly the entire dolostone sequence is deposited in each location before the sea level rises to precipitate carbonate in the next shallower outcrop location. Lame Horse Gully is the one example (out of 41 sections) where the geographic location, sedimentology and $\delta^{13}C$ values together do not match the documented patterns elsewhere. Mapping and further sampling of this region is a target for future work.

Sections throughout the south and central regions share similar isotopic ranges to one another, suggesting that the majority of sections flooded synchronously. The minimal lateral isotopic gradients imply that only small-scale glacial erosion and salt diapir related relief caused minor diachroneity. This interpretation is in agreement with the sedimentology, which identifies these regions to have broadly similar, but locally variable, water depths. Towards the shallowest palaeobathymetric setting to the south, the overall $\delta^{13}C$ starting values should be relatively lighter compared to those in the north (Hoffman et al., 2007) (Fig. 10C). However, the $\delta^{13}C$ starting values for some sections are as heavy as those in the north, suggesting that glacioeustatic flooding happened in the central and southern Flinders Ranges before the north, and yielding a result that is inconsistent with inferred palaeobathymetry. If the central Flinders Ranges underwent salt withdrawal and deep subsidence during a sedimentary hiatus at peak glaciation, then this mismatch between underlying facies and overlying $\delta^{13}C$ values in the Nuccaleena Fm could be rationalised. However, this hypothesis is inconsistent with the facies interpretations of the cap dolostone itself in the central region, due to the absence of sheet-crack cements. Also, the hypothesis would require the ice-contact glacial diamictites to represent the onset and not termination of the ice age. The similar basal isotopic values in the north, central and south remain enigmatic.

Hoffman et al. (2007), Hoffman (2010) attributed a 4.4‰ decline in $\delta^{13}C$ values in the Keilberg Fm, Namibia, to a continual increase in temperature, rather than a change in the isotopic composition of seawater, over the time taken for post-glacial flooding. The Nuccaleena Fm cap dolostone records a similar ~4.5‰ decline in $\delta^{13}C$ values. However, this decrease would require an unrealistic >38 °C increase in temperature with time. In addition, the $\delta^{13}C$ values in the central and southern regions are heavier (Fig. 10C). If an influx of cold, glacial meltwater inundated the platform it would decrease temperature (and salinity), and thus increase the fractionation and the $\delta^{13}C$ values on the platform. However, such an extreme temperature gradient would be very difficult to maintain where giant waves are present, suggesting rapid mixing throughout both regions. Furthermore, the average $\delta^{18}O$ isotope values become progressively heavier towards the south and, therefore, are inconsistent with an influx of glacial meltwater. Temperature-dependent isotopic fractionation cannot be the only control determining the isotopic variability within the Nuccaleena Fm.

East Mundawertina and Mundawertina Well are two of the deepest sections in the ARC and are overlain by grey limestone ribbonite. Regardless of the mechanism for deposition, the absence of limestone to the south of Mt. Fitton anticline may be because silt overwhelmed deposition in the proximal, shallow regions, so that only the deepest setting to the north preserved limestone deposition (Fig. 1C2). In an isochronous model, the limestone is deposited simultaneously across the platform after the dolostone deposition. For a diachronous cap carbonate, dolostone is deposited from the incipient glacial meltwater plume that mixes with the ocean to create a mixed surface layer (Fig. 1C1). As sea level rises, the underlying thermocline, which separates the mixed layer from the deep water below, migrates upslope and deposits limestone (Fig. 1C2). Therefore, whilst dolostone is being deposited on the bank, limestone is simultaneously being deposited on the slope (Fig. 1C3).

We propose that the limestone is correlative by lithofacies to the cap limestones documented above other younger Cryogenian cap dolostones around the world. However, the Mundawertina Mb is not isotopically similar. The limestone is ~2‰ lighter than the other younger Cryogenian cap carbonates (Fig. 10C), suggesting that either a lateral gradient existed between these two cap limestones, or that the limestone was not deposited synchronously around the world. The Mundawertina Well may represent some of the deepest limestone outcrops of the younger Cryogenian cap carbonate ever studied and would represent the oldest global limestone in a diachronous model.

7. Conclusion

Complex palaeogeography and salt diapirism preclude the use of a simple isolated carbonate platform to quantify palaeo-water depths across the Adelaide Rift Complex. However, we do document the sedimentological and geochemical variability of the cap dolostone over a range of water depths (<200 to >400 m) within a 45000 km^2 single basin. We have illustrated that the δ^{13}C trajectory of the cap dolostone is remarkably uniform, whilst the starting values for individual isotope trends vary dramatically over different spatial scales. Much of the δ^{13}C variability across the ARC can be explained by pairing sedimentological observations and structural interpretations of palaeobathymetry to the diachronous model for cap deposition. The northern ARC shows that cap dolostone deposition tracked the glacioeustatic sea-level rise over a series of half-grabens that deepened to the north and recorded the isotopic evolution of the deglacial ocean. However, the central Flinders Ranges δ^{13}C record suggests nearly isochronous deposition that occurred earlier than expected for the paleobathymetry of the Central Flinders shelf. Furthermore, changes in δ^{13}C are too large to explain entirely with temporal and lateral temperature gradients. Therefore, only about half of the variance in δ^{13}C across the Adelaide Rift Complex can be ascribed to diachronous sedimentation and sea water temperature evolution during deglaciation. New studies that pair sedimentological and chemostratigraphic observations across a range of water depths on other continents will be required to make the next leap in our understanding of cap dolostone deposition, the duration of deglaciation, and the carbon isotope evolution of post-glacial oceans.

Acknowledgements

Field and stable isotope work was supported by NSF grant EAR-0842946 awarded to Maloof. Francis Macdonald and Tony Prave gave constructive reviews of the manuscript. We also benefitted from useful discussions with Sarah Fawcett, John Higgins, Jon Husson and Nick Swanson-Hysell. Fiona Best, Justin Strauss, Nick Swanson-Hysell and Nora Xu provided enthusiastic assistance in the field. Darren Crawford and Arthur Coulthard gave invaluable help accessing the Flinders Ranges and Vulkathunha-Gammon Ranges National Parks, respectively. We are very grateful to the landowners and pastoralists for land access. Matt Hurtgen kindly provided the samples for Chambers Gorge. Will Jacobsen, Justin Strauss, Lija Treibergs and Nora Xu helped with sample preparation. Lora Wingate and Kacey Lohmann performed the stable isotope measurements at the University of Michigan.

Appendix A. Supplementary data

Supplementary data associated with this article can be found, in the online version, at doi:10.1016/j.epsl.2010.03.031.

References

Aitken, J., 1991. The Ice Brook Formation and post-Rapitan, late Proterozoic glaciation, Mackenzie Mountains, Northwest Territories. Geol. Surv. Can. Bull. 404, 43.
Allen, P., Hoffman, P., 2005. Extreme winds and waves in the aftermath of a Neoproterozoic glaciation. Nature 433, 123–127.
Bowring, S., Grotzinger, J., Condon, D., Ramezani, J., Newall, M., Allen, P., 2007. Geochronological constraints on the chronostratigraphic framework of the Neoproterozoic Huqf Supergroup, Sultanate of Oman. Am. J. Sci. 307, 1097–1145.
Calver, C., 2000. Isotope stratigraphy of the Ediacaran (Neoproterozoic III) of the Adelaide rift complex, Australia, and the overprint of water column stratification. Precambrian Res. 100, 121–150.
Coats, R., 1981. Late Proterozoic (Adelaidean) tillites of the Adelaide Geosyncline. In: Hambrey, M., Harland, W. (Eds.), Earth's Pre-Pleistocene Glacial Record. Cambridge University Press, pp. 537–548.
Coats, R., Callen, R., Williams, A., Thompson, B., 1973. Copley 1:250,000 geological map sheet. Tech. Rep., Geological Survey of South Australia, Department of Mines Adelaide.
Condon, D., Zhu, M., Bowring, S., Wang, W., Yang, A., Jin, Y., 2005. U–Pb ages from the Neoproterozoic Doushantuo Formation, China. Science 308, 95–98.
Dyson, I., 1992. Stratigraphic nomenclature and sequence stratigraphy of the lower Wilpena Group, Adelaide Geosyncline: the Sandison Subgroup. Geol. Surv. S. Aust. Q. Geol. Notes 122, 2–13.
Embleton, B., Williams, G., 1986. Low paleolatitude of deposition for Late Precambrian periglacial varvites in South Australia: implications for paleoclimatology. Earth Planet. Sci. Lett. 79, 419–430.
Evans, D., 2000. Stratigraphic, geochronological, and paleomagnetic constraints upon the Neoproterozoic climatic paradoxes. Am. J. Sci. 300, 347–443.
Eyles, C.H., Eyles, N., Grey, K., 2007. Palaeoclimate implications from deep drilling of Neoproterozoic strata in the Officer Basin and Adelaide Rift Complex of Australia; a marine record of wet-based glaciers. Palaeogeogr. Palaeoclimatol. Palaeoecol. 248 (3–4), 291–312.
Fanning, M., 2006. Constraints on the timing of the Sturtian glaciation from southern Australia; i.e., for the true Sturtian. Geological Society of America Abstracts with Programs, vol. 38, p. 115.
Fanning, C., Ludwig, K., Forbes, B., Preiss, W., 1986. Single and multiple grain U–Pb zircon analyses for the Early Adelaidean Rook Tuff, Willouran Ranges, South Australia. Abstr. Geol. Soc. Aust. 15, 71–72.
Font, E., Nedelec, A., Trindade, R.I.F., Macouin, M., Charriere, A., 2006. Chemostratigraphy of the Neoproterozoic Mirassol d'Oeste cap dolostones (Mato Grosso, Brazil): an alternative model for Marinoan cap dolostone formation. Earth Planet. Sci. Lett. 250 (1–2), 89–103.
Forbes, B., Preiss, W., 1987. Stratigraphy of the Wilpena Group. In: Preiss, W. (Ed.), The Adelaide Geosyncline of South Australia, Late Proterozoic stratigraphy, sedimentation, palaeontology and tectonics: Geological Survey of South Australia, 53, pp. 211–248.
Gammon, P., McKirdy, D., Smith, H., 2005. The timing and environment of teepee formation in a Marinoan cap carbonate. Sed. Geol. 177, 195–208.
Giddings, J., Wallace, M., 2009. Facies-dependent δ^{13}c variation from a Cryogenian platform margin, South Australia: evidence for stratified Neoproterozoic oceans? Palaeogeogr. Palaeoclimatol. Palaeoecol. 271, 196–214.
Halverson, G., Maloof, A., Hoffman, P., 2004. The Marinoan glaciation (Neoproterozoic) in northeast Svalbard. Basin Res. 16, 297–324.
Halverson, G., Hoffman, P., Maloof, A., Schrag, D., Rice, A.H.N., Bowring, S., Dudas, F., 2005. Toward a Neoproterozoic composite carbon-isotope record. Geol. Soc. Am. Bull. 117, 1181–1207.
Higgins, J., Schrag, D., 2003. The aftermath of a snowball Earth. Geochem. Geophys. Geosyst. 4 (3), 1028. doi:10.1029/2002GC000403.
Hoffman, P., 2005. On Cryogenian (Neoporterozoic) ice-sheet dynamics and the limitations of the glacial sedimentary record. S. Afr. J. Geol. 108, 557–576.
Hoffman, P., 2010. Strange bedfellows: glacial diamictite and cap carbonate from the Marinoan (635 Ma) glaciation in Nambia. Sedimentology Special Decadal Issue.
Hoffman, P., Li, Z., 2009. A palaeogeographic context for Neoproterozoic glaciation. Palaeogeogr. Palaeoclimatol. Palaeoecol. 277, 158–172.
Hoffman, P., Kaufman, A., Halverson, G., Schrag, D., 1998. A Neoproterozoic snowball Earth. Science 281, 1342–1346.
Hoffman, P., Halverson, G., Grotzinger, J., 2002. Are Proterozoic cap carbonates and isotopic excursions a record of gas hydrate destabilization following Earth's coldest intervals? Comment and reply. Geology 286–287 (March).
Hoffman, P., Halverson, G., Domack, E., Husson, J., Higgins, J., Schrag, D., 2007. Are basal Ediacaran (635 ma) post-glacial "cap dolostones" diachronous? Earth Planet. Sci. Lett. 258, 114–131.
Hoffmann, K.-H., Condon, D., Bowring, S., Crowley, J., 2004. A U–Pb zircon date from the Neoproterozoic Ghaub Formation, Namibia: constraints on Marinoan glaciation. Geology 32, 817–820.
Hurtgen, M.T., Halverson, G.P., Arthur, M.A., Hoffman, P.F., 2006. Sulfur cycling in the aftermath of a 635-Ma snowball glaciation: evidence for a syn-glacial sulfidic deep ocean. Earth Planet. Sci. Lett. 245 (3–4), 551–570.
Hyde, W., Crowley, T., Baum, S., Peltier, W., 2000. Neoproterozoic 'snowball Earth' simulations with a coupled climate/ice-sheet model. Nature 405, 425–429.
James, N., Narbonne, G., Kyser, T., 2001. Late Neoproterozoic cap carbonates: Mackenzie Mountains, northwestern Canada: precipitation and global glaciation. Can. J. Earth Sci. 38, 1229–1262.
Jenkins, R., 1990. The Adelaide Fold Belt: tectonic reappraisal. Geol. Soc. Aust. Spec. Publ. 16, 395–420.
Jerolmack, D., Mohrig, D., 2005. Formation of Precambrian sediment ripples. Nature 436, E1.
Jiang, G., Kennedy, M., Christie-Blick, N., 2003. Stable isotopic evidence for methane seeps in Neoproterozoic postglacial cap carbonates. Nature 426, 822–826.
Jiang, G., Kennedy, M., Christie-Blick, N., Wu, H., Zhang, S., 2006. Stratigraphy, sedimentary structures, and textures of the late Neoproterozoic Doushantuo cap carbonate in South China. J. Sed. Res. 76, 978–995.
Kaufman, A., Hayes, J., Knoll, A., Germs, G., 1991. Isotopic compositions of carbonates and organic carbon from upper Proterozoic successions in Namibia: stratigraphic variation and the effects of diagenesis and metamorphism. Precambrian Res. 49, 301–327.
Kaufman, A., Knoll, A., Narbonne, G., 1997. Isotopes, ice ages, and terminal Proterozoic Earth history. Proc. Natl. Acad. Sci. 95, 6600–6605.
Kendall, C., Warren, J., 1987. A review of the origin and setting of teepees and their associated fabrics. Sedimentology 34, 1007–1028.
Kennedy, M., 1996. Stratigraphy, sedimentology, and isotopic geochemistry of Australian Neoproterozoic postglacial cap dolostones: deglaciation, δ^{13}C excursions, and carbonate precipitation. J. Sed. Res. 66 (6), 1050–1064.
Kennedy, M., Runnegar, B., Prave, A., Hoffman, K., Arthur, M., 1998. Two or four Neoproterozoic glaciations? Geology 26, 1059–1063.

Kennedy, M., Christie-Blick, N., Sohl, L., 2001. Are proterozoic cap carbonates and isotopic excursions a record of gas hydrate destabilization following Earth's coldest intervals? Geology 29 (5), 443–446.
Kennedy, M., Mrofka, D., von der Borch, C., 2008. Snowball Earth termination by destabilization of equatorial permafrost methane clathrate. Nature 453, 642–645.
Kilner, B., Mac Niocaill, C., Brasier, M., 2005. Low-latitude glaciation in the Neoproterozoic of Oman. Geology 33 (5), 413–416.
Knauth, L., Kennedy, M., 2009. The late Precambrian greening of the Earth. Nature 460, 728–732 (August).
Knoll, A., Walter, M., Narbonne, G., Christie-Blick, N., 2006. The Ediacaran Period: a new addition to the geologic time scale. Lethaia 39, 13–30.
Lemon, N., Gostin, V., 1990. Glacigenic sediments of the late Proterozoic Elatina Formation and equivalents, Adelaide Geosyncline, South Australia. In: Jago, J., Moore, P. (Eds.), The Evolution of a Late Precambrian–Early Palaeozoic Rift Complex, 16. Geological Society of Australia, pp. 149–164.
Macdonald, F., Schmitz, M., Crowley, J., Roots, C., Jones, D., Maloof, A., Strauss, J., Cohen, P., Johnston, D., Schrag, D., 2010. Calibrating the Cryogenian. Science 327, 1241–1243.
McLaren, S., Dunlap, W., Sandiford, M., McDougall, I., 2002. Thermochronology of high heat-producing crust at Mount Painter, South Australia: Implications for tectonic reactivation of continental interiors. Tectonics 21 (4), 1–18.
Myrow, P., Tice, L., Archuleta, B., Clark, B., Taylor, J., Ripperdan, R., 2004. Flat-pebble conglomerate: its multiple origins and relationship to metre-scale depositional cycles. Sedimentology 51, 973–996.
Paul, E., Flottmann, T., Sandiford, M., 1999. Structural geometry and controls on basement-involved deformation in the northern Flinders Ranges, Adelaide Fold Belt, South Australia. Aust. J. Earth Sci. 46, 343–354.
Peltier, W., Tarasov, G., Vettoretti, L., Solheim, L., 2004. Climate dynamics in deep time: modelling the "snowball bifurcation" and assessing the plausibility of its occurrence. In: Jenkins, G., McMenamin, M., McKey, C., Sohl, L. (Eds.), The Extreme Proterozoic: Geology, Geochemistry and Climate, 146. American Geophysical Union, pp. 107–124.
Plummer, P., 1979. Note on the palaeoenvironmental significance of the Nuccaleena Formation (upper Precambrian), central Flinders Ranges, South Australia. J. Geol. Soc. Aust. 25, 395–402.
Prave, A., 1999. Two diamictites, two cap carbonates, two δ^{13}c excursions, two rifts: the Neoproterozoic Kingston Peak Formation, Death Valley, California. Geology 27, 339–342.
Preiss, W., 1987. Stragraphic nomenclature and classification. In: Preiss, W. (Ed.), The Adelaide Geosyncline of South Australia, Late Proterozoic Stratigraphy, Sedimentation, Palaeontology and Tectonics: Geological Survey of South Australia, 53.
Preiss, W., 2000. The Adelaide Geosyncline of South Australia and its significance in Neoproterozoic continental reconstruction. Precambrian Res. 100, 21–63.
Preiss, W., Robertson, R., 2002. South Australian mineral explorers guide. Tech. Rep. PIRSA.
Raub, T., Evans, D., 2006. Magnetic reversals in basal Ediacaran cap carbonates: a critical review. Eos Trans. AGU, Vol. 87(36), p. GP41B-02.
Raub, T., Evans, D., 2008. Paleolatitudes of Neoproterozoic snowball glacial deposits: biases and synthesis. 33rd International Geological Congress, Oslo (Abstract CGC-04) (August).
Raub, T., Evans, D., Smirnov, A., 2007. Siliciclastic prelude to Elatina–Nuccaleena deglaciation: lithostratigraphy and rock magnetism of the base of the Ediacaran system. In: Vickers-Rich, P., Komarower, P. (Eds.), The Rise and Fall of the Ediacaran Biota. Vol. 286. Geological Society London, Special Publication, pp. 53–76.
Rieu, R., Allen, P., Cozzi, A., Kosler, J., Bussy, F., 2007. A composite stratigraphy for the Neoproterozoic Huqf Supergroup of Oman: integrating new litho-, chemo- and chronostratigraphic data of the Mirbat area, southern Oman. J. Geol. Soc. London 164, 997–1009.
Schmidt, P., Williams, G., 1995. The Neoproterozoic climatic paradox: equatorial palaeolatitude for Marinoan glaciation near sea level in South Australia. Earth Planet. Sci. Lett. 134, 107–124.
Schmidt, P., Williams, G., Embleton, B., 1991. Low palaeolatitude of Late Proterozoic glaciation: early timing of remanence in haematite of the Elatina Formation, South Australia. Earth Planet. Sci. Lett. 105, 355–367.
Schmidt, P., Williams, G., McWilliams, M., 2009. Palaeomagnetism and magnetic anistropy of late Neoproterozoic strata, South Australia: implications for the palaeolatitude of late Cryogenian glaciation, cap carbonate and the Ediacaran System. Precambrian Res. 174, 35–52.
Shields, G., 2005. Neoproterozoic cap carbonates: a critical appraisal of existing models and the plumeworld hypothesis. Terra Nova 17, 299–310.
Sohl, L., Christie-Blick, N., Kent, D., 1999. Paleomagnetic polarity reversals in Marinoan (ca. 600 Ma) glacial deposits of Australia: implications for the duration of low-latitude glaciation in Neoproterozoic time. Geol. Soc. Am. Bull. 111, 1120–1139.
Thomson, B., Coats, R., Mirams, R., Forbes, B., Dalgarno, C., Johnson, J., 1964. Precambrian rock groups in the Adelaide Geosyncline: new subdivision. Q. J. Geol. Surv. S. Aust. 9, 1–19.
Trindade, R., Font, E., D'Agrella-Filho, M., Nogueira, A., Riccomini, C., 2003. Low-latitude and multiple geomagnetic reversals in the Neoproterozoic Puga cap carbonate, Amazon craton. Terra Nova 15 (6), 441–446.
Williams, G., 1977. Late Precambrian dolomites, Vendian glaciation, and synchroneity of Vendian glaciations: a discussion. J. Geol. 85, 250–252.
Williams, G., 1979. Sedimentology, stable-isotope geochemistry and palaeoenvironment of dolostones capping late Precambrian glacial sequences in Australia. J. Geol. Soc. Aust. 26, 377–386.
Williams, G., Gostin, V., McKirdy, D., Preiss, W., 2008. The Elatina glaciation, late Cryogenian (Marinoan Epoch), South Australia: Sedimentary facies and paleoenvironments. Precambrian Res. 163, 307–331.
Wingate, M., Cambell, I., Compston, W., Gibson, G., 1998. Ion microprobe U–Pb ages for Neoproterozic basaltic magmatism in south-central Australia and implications for the breakup of Rodinia. Precambrian Res. 100, 335–357.
Xiao, S., Bao, H., Wang, H., Kaufman, A., Zhou, C., Li, G., Yuan, X., Ling, H., 2004. The Neoproterozoic Quruqtagh Group in eastern Chinese Tianshan: evidence for a post-Marinoan glaciation. Precambrian Res. 130, 1–26.